Utrecht University

Institute for
Marine and Atmospheric
research Utrecht

Multiple equilibria of the Late Eocene ocean circulation

and their role in the Eocene-Oligocene transition

Master thesis

E.B. Sipma

Study: Climate Physics

Supervisor:

dr. A.S. von der Heydt

Institute for Marine and Atmospheric Research Utrecht

Department of Physics

June 11, 2021

Abstract

One of the largest shifts in climate in the Cenozoic (last 66 million years) occurred around the Eocene-Oligocene transition (EOT, 33.9 Ma) and is marked by global cooling and the sudden appearance of a large continental ice sheet on Antarctica. The two main proposed explanations of this climatic shift are a decline in atmospheric CO_2 and changes in ocean gateways influencing ocean circulation, though the exact mechanisms behind this are still debated.
This thesis focusses on the idea that the rapid cooling could have been initiated by a shift in the Meridional Overturning Circulation (MOC) from one equilibrium state to another. To study this, equilibrium ocean states are obtained with the ocean-only fully implicit thermohaline circulation model (THCM), using two different paleobathymetries (40 Ma and 30 Ma) and two different patterns of surface forcing representing different CO_2 levels.
Under restoring boundary conditions a strong southern sinking MOC-pattern is found, which is in line with fully coupled Global Circulation Model (GCM) simulations, only stronger. When the upper layer salinity forcing is mirrored at the equator, a MOC-pattern with only northern sinking is found. Starting from these solutions, bifurcation diagrams of the equilibrium ocean circulation under changing freshwater flux forcing are calculated. In these bifurcation diagrams a range of different MOC-states are found to occur, including southern sinking, bipolar sinking and northern sinking states, most of which are connected. There is a range of boundary conditions for which multiple MOC-states occur, suggesting that a shift between two of these patterns, induced by e.g. random atmospheric fluctuations, could be possible. Specifically, a southern sinking MOC-state with weak positive (northern) overturning in the Atlantic is found under the same boundary conditions as the strong fully southern sinking pattern. A shift between these two MOC-states seems to agree with the proposed onset of the Atlantic Meridional Overturning Circulation (AMOC) around time of EOT, which could have induced southern hemisphere cooling. Furthermore, the observed meridional heat transport suggests that this shift in MOC-states would result in a cooler southern and warmer northern hemisphere. Since the results were found to be relatively similar for both paleobathymetries and surface forcings used, the possibility of a shift in MOC-pattern around the time of the EOT seems to be relatively independent of the exact timing of gateway openings and of CO_2 levels.

Contents

1 Introduction

Earth's climate has changed enormously over time, on a wide variety of timescales. Understanding why and how these changes have occurred in the past provides useful insights to help understand how climate might change in the future. The last 66 million years of Earth's history make up the Cenozoic era. The climate in the first half of the Cenozoic is characterised by a general warming trend, peaking at the Early Eocene Climatic optimum (EECO, $\sim$ 52-50 Ma). The climate at this time is a greenhouse climate, with e.g. a subtropical climate in North America, Eurasia and even some locations in the Arctic without the presence of major ice sheets (Stanley, 2008; Sluijs et al., 2006). After the EECO to the present, the climate is characterised by a general cooling trend and a transition from the greenhouse climate in the first part of the Cenozoic to the icehouse climate as we know now. This general cooling trend is evidenced by an increase in δ^{18}O values from deep-sea sediment cores (Westerhold et al., 2020; Zachos et al., 2001). An increase in δ^{18}O values reflects an increase in ice volume and/or a decrease in deep-sea temperature. Apart from these general cooling and warming trends, several rapid (10^3 to 10^5 yr) shifts in climate from a warmer to a cooler climate and vice versa have taken place during the Cenozoic (Westerhold et al., 2020; Zachos et al., 2001).
One of the largest of these shifts occurred around the Eocene-Oligocene Transition (EOT, 33.9 Ma) and coincides with the sudden appearance of a large continental ice sheet on Antarctica (Zachos et al., 2001). The Eocene-Oligocene boundary is marked by a widespread extinction (Prothero, 1994). The shift in climate is indicated by an ($\sim$ 400 kyr) increase in δ^{18}O values in deep-sea sediments, referred to as the Early Oligocene Glacial Maximum (EOGM) or Oi-1 (Hutchinson et al., 2020; Zachos et al., 2001). In high resolution (up to 2 kyr) tropical Pacific δ^{18}O records this shift is found to occur in two $\sim$ 40 kyr steps separated by plateau of $\sim$ 200 kyr, ending in an overshoot (maximum) (Coxall et al., 2005). The shift in δ^{18}O coincides with a two-step $>$ 1 km deepening of the calcite compensation depth (CCD) and a two step increase in δ^{13}C (with a $<$ 10 kyr lag) (Coxall et al., 2005). A possible explanation for the decrease in CCD is the ice expansion on Antarctica and sea level fall, inducing a shift in $CaCO_3$ sedimentation from shelf to deep ocean basins (Coxall et al., 2005; Pälike et al., 2012). Either no cooling or cooling of a few degrees in the deep sea is observed in Mg/Ca records. Possibly in the records that do not show cooling, the cooling is masked by increasing pH/$[CO_3^{2-}]$, associated with the decrease in CCD (Lear et al., 2008; Bohaty et al., 2012; Coxall et al., 2005). The first step of the shift in δ^{18}O is thought to be mainly due to cooling, while the second step is mainly due to ice sheet growth (Katz et al., 2008; Pearson et al., 2009)

There are several possible explanations of the occurrence of the climatic shift around the EOT. The first is the opening of ocean gateways (e.g. the Tasman gateway and Drake passage), changing the ocean circulation, for example enabling an Antarctic Circumpolar Current (ACC), which in the present-day climate prevents meridional heat transport across it towards the Antarctic continent, consequentially isolating Antarctica from the rest or the world. The precise timing of the opening of these gateways is, however, difficult to determine (Livermore et al., 2005; Scher and Martin, 2006; Pfuhl and McCave, 2005) and the decrease in heat transport due to the ACC has been found to be much too weak to cause a significant change in Antarctic climate (Huber and Nof, 2006).
Another way to explain the climatic shift, is that atmospheric CO_2 levels might have been declining past a threshold at the time of the EOT, which could have triggered a rapid increase in ice sheet volume trough positive feedback (DeConto and Pollard, 2003). Orbital forcing is thought to aid the initiation and rapid increase of the ice sheet, as at the time of the EOT eccentricity is low and obliquity has a low amplitude, dampening seasonality such that the summers are relatively cold (Zachos et al., 2001; Coxall et al., 2005). While this could explain the second step in the shift in δ^{18}O, which is thought to be mainly due to rapid ice sheet growth, the cause of the first step, which is thought to be mainly due to cooling, still needs to be considered. A possibility is that the decrease in CO_2

(and perhaps other greenhouse gases) at the time of the EOT reduced the greenhouse effect, thus inducing global cooling (Pearson et al., 2009) The timing and temporal structure of such a decrease is, however, not easily identifiable in data since available CO_2 (and greenhouse gas) records are quite uncertain and generally do not have a high enough resolution around the EOT (Pearson et al., 2009). Furthermore, it is unknown what would have caused such a relatively large decrease in CO_2.

In addition to a decrease in CO_2, a possible cause of the rapid cooling could be a shift in ocean circulation from one equilibrium state to another (Tigchelaar et al., 2011). This idea is based on the existence of multiple equilibria in the Meridional Overturning Circulation (MOC). As the MOC regulates the meridional heat transport, a different pattern in MOC has a significant effect on regional climates. Apart from heat transport, the MOC influences nutrient transport and global carbon cycling as well (see e.g. Cheng et al. (2013); Sabine et al. (2004)). With model simulations using a simple continental geometry von der Heydt and Dijkstra (2008) found that in an east-west symmetric configuration four possible MOC patterns can occur; a northern sinking state (deep water formation in North Atlantic and North Pacific), a southern sinking state (deep water formation in the Southern Ocean only), a conveyor state (deep water formation in the North Atlantic and Southern Ocean, present-day state) and an inverse conveyor state (deep water formation in the North Pacific and Southern Ocean). By introducing an asymmetry based on Oligocene continental geometry, some of the MOC patterns were found to be more likely than others.
During the Eocene, the suggested MOC-pattern is one with deep water formation predominantly in the Southern Ocean and North Pacific (Hutchinson et al., 2020; Ferreira et al., 2018; Hutchinson et al., 2018). There is evidence from proxy records that suggests the onset or strengthening of the Atlantic Meridional Overturning Circulation (AMOC) around the time of the EOT (Hutchinson et al., 2020; Via and Thomas, 2006; Borrelli et al., 2014). A possible cause for the onset of deep water formation in the North Atlantic is the tectonic deepening of the Greenland-Scotland ridge that separates the Greenland-Norwegian sea from the North Atlantic, such that water can be exchanged and the Northern seas become a site of deep water formation (Via and Thomas, 2006). Another possible cause is the closure of the Arctic-Atlantic gateway, blocking the inflow of fresh water from the Arctic to the Atlantic and allowing an AMOC to develop (Hutchinson et al., 2019). The deep water formation in the North Pacific is found to decrease around the time of the EOT (McKinley et al., 2019; Hutchinson et al., 2019; Fontorbe et al., 2017; Thomas et al., 2008).
Tigchelaar et al. (2011) argued that the first step in the shift in $\delta^{18}O$ might be due to a shift in MOC pattern from southern sinking to sinking at both poles (conveyor/inverse conveyor). As the North Atlantic, the additional source of deep water formation in the new pattern, was found to have lower Sea Surface Temperatures (SST) than the Southern Ocean, this results in significant cooling of the deep sea and increasing $\delta^{18}O$. The density perturbation that is used in model studies (von der Heydt and Dijkstra, 2008; Tigchelaar et al., 2011) to induce the switch to a different MOC pattern, may in reality be caused by (random) atmospheric fluctuations. Alternatively, changes in paleobathymetry influencing the preference of the MOC patterns may induce a switch in MOC pattern.

Some research has been done concerning the effect of (paleo)bathymetry on the ocean circulation pattern. Using two realistic, slightly differing late Eocene ($\sim$ 38 Ma) paleobathymetries, one based on a hotspot reference frame (HS) and one on a paleomagnetic reference frame (PM), Baatsen et al. (2018) found a different MOC pattern in each case. This shows that multiple MOC patterns can be found for a realistic late Eocene continental geometry. Huisman et al. (2012) argued that for the present-day bathymetry there seems to be a preference for North Atlantic deep water formation, as even when the Sea Surface Salinity (SSS) pattern of the Atlantic and Pacific is switched, a conveyor solution exists.
In Mulder et al. (2017) a method is introduced to directly compute equilibrium three-dimensional ocean flow under a deformation of bathymetry. In the calculated ocean circulation patterns from 65 Ma until now, in steps of 5 Ma, only southern sinking MOC-states were found. This is, however, a result of the restoring boundary conditions, where surface temperature and salinity are being restored to predefined temperature and salinity field, that are used as forcing at the ocean surface.

Furthermore, the surface forcing prescribed is an idealised zonally averaged pattern. Similar techniques are used in Dijkstra and Weijer (2005) to study the present-day global ocean circulation. Here multiple equilibria, a solution with strong northern overturning and one with hardly any overturning in the Atlantic, were found to occur under a freshwater flux perturbation in the North Atlantic.

In this project, a method is used that is similar to the method used in Dijkstra and Weijer (2005) and Mulder et al. (2017) and is extended upon the restoring solutions found in Mulder et al. (2017) by introducing a more realistic forcing at the ocean surface and by introducing mixed boundary conditions. As with mixed boundary conditions the upper layer salinity is no longer constrained by restoring to a prescribed field, more freedom is allowed which increases the realism of the solution. Since the method directly calculates the three dimensional equilibrium ocean circulation pattern, no long spin-up time is needed to reach an equilibrium, as would be the case with a time stepping method. Thus it is possible to study how the equilibrium ocean circulation pattern changes under a change in parameter, such as the magnitude of a perturbation in the freshwater flux that is used as mixed boundary condition. There is, however, a price to pay: as the method requires large matrices to be solved (iteratively), a lot of memory is needed and if the iteration does not converge, no solution can be obtained.
The aim of this project is to study the global ocean circulation, the existence of multiple equilibrium MOC-states and the possibility of a shift from one equilibrium MOC-state to another around the time of the EOT. Additionally, the effect of paleobathymetry on global ocean circulation and the possible preference for a certain equilibrium MOC-state is studied. This to help understand whether a shift in ocean circulation state might have occurred around the EOT, what the mechanisms might be behind such a shift and the possible effects of a shift in ocean circulation state on the climate.
In order to study the meridional overturning circulation around the time of the Eocene-Oligocene Transition, two different paleobathymetries are used as boundary condition, one at 40 Ma and one at 30 Ma. To create relatively realistic atmospheric forcing, surface forcing patterns are taken from equilibrium states obtained with the Community Earth System Model (CESM) in Baatsen (2019); Baatsen et al. (2020). Using restoring boundary conditions, equilibrium solutions are obtained for both paleobathymetries. Then is switched to mixed boundary conditions, where the freshwater flux diagnosed from the obtained restoring equilibrium solutions is used as a boundary condition instead of surface layer salinity. Connections between the obtained restoring equilibrium MOC-states and the possible connections to other MOC-states are studied using continuations in different parameters, for example, the magnitude of a perturbation in freshwater flux or a transition parameter to smoothly change from one freshwater flux forcing field to another.
More information about the model, surface forcing and other methods is given in chapter 2. The results of the simulations are given in chapter 3 and discussed in chapter 4. The conclusions are found in chapter 5.

2 Methods

This section gives a description of the methods applied to perform simulations and to analyse the results of these simulations. Firstly, a description of the model is given in section 2.1. The model setup is explained, along with a brief explanation of how the model works, the effect of some of the parametrisations and parameter choices and the definitions of several diagnostics and parameters. Secondly, the paleobathymetries that are considered in the simulations are given and discussed in section 2.2, along with a description of how the ocean basins are defined. Thirdly, a description of the surface forcing, how it is obtained and how modified forcing fields are constructed is given in section 2.3. Lastly, the equation of state in the model and how its coefficients are modified to better approximate the density for the warmer climate around the Eocene-Oligocene Transition (EOT) is discussed in section 2.4.

2.1 The ocean model

In this project the fully implicit thermohaline circulation model (THCM) is used, of which a full description can be found in de Niet et al. (2007). The governing equations of this ocean model are the hydrostatic, primitive equations in spherical coordinates (longitude ϕ, latitude θ and depth z) that describe the evolution of the zonal, meridional and vertical ocean velocities u, v and w, pressure p, temperature T and salinity S. Different from the present-day case the model includes a bathymetry and continental geometry representative of the Late Eocene and Early Oligocene as described in section 2.2. Slip and no-flux conditions are assumed at the bottom boundary, no-slip and no-flux conditions at the lateral boundaries.
At the ocean-atmosphere boundary, the flow is forced with a prescribed wind stress field (see section 2.3). For temperature and salinity two types of boundary conditions are used; restoring and mixed boundary conditions. In case of restoring boundary conditions, the temperature and salinity of the upper layer are assumed to restore to a prescribed temperature and salinity field (see section section 2.3) with a timescale of $\tau_T = \tau_S = 75$ days. For mixed boundary conditions a freshwater flux is prescribed while upper layer temperature is again assumed to be restoring. This freshwater flux is diagnosed from a previously obtained solution under restoring boundary conditions and is proportional to the difference between the upper layer salinity forcing and the upper layer salinity of the restoring solution. Per definition the global average freshwater flux is zero. Wind stress, temperature and salinity forcing are all represented as a body force acting on the upper layer, hence slip and no-flux conditions are assumed at the surface.
The model is set up with a rectangular grid with a horizontal resolution of 3° (grid of $N \times M = 120 \times 54$, domain 81°S - 81°N, 0°E - 360°E) and $L = 12$ non-equidistant vertical levels, where the layer thickness increases from 94.8 m for the upper layer to 786.2 m for the deepest layer. The default values of fixed parameters used in the model computations are given in Table 2.1.

2.1.1 Continuation Methods

As not everyone is familiar with continuation methods, a brief explanation of how these methods are implemented in the model is given below. A more elaborate explanation is given in e.g. Dijkstra and Weijer (2005); de Niet et al. (2007); Thies et al. (2009)
The set of governing equations is spatially discretised using a second-order accurate finite volume method. This is done on a staggered Arakawa B-grid in the horizontal ($i = 1, ..., N$, $j = 1, ..., M$) and a C-grid in the vertical ($k = 1, ..., L$), see Figure 2.1. The result is a system of six equations with boundary conditions that can be separated into a part (left hand side) that contains a time derivative

Table 2.1: Default values of fixed parameters used in model computations

Symbol	Value	Unit	Name
U	0.1	$[ms^{-1}]$	Velocity scale
D	5.0×10^3	[m]	Basin depth
Ω	7.292×10^{-5}	$[s^{-1}]$	Earth's angular velocity
g	9.8	$[ms^{-2}]$	Standard acceleration due to gravity
r_0	6.37×10^6	[m]	Radius of the Earth
T_0	15.0	[°C]	Reference temperature
S_0	35.0	[psu]	Reference salinity
ρ_0	1.024×10^3	$[kgm^{-3}]$	Reference density
F_0	1.0×10^{-7}	$[ms^{-1}]$	Freshwater flux amplitude
τ_T, τ_S	75	[days]	Restoring timescale of upper layer temperature/salinity
α_T	2.16×10^{-4}	$[K^{-1}]$	Volumetric expansion coefficient (temperature)
α_S	6.42×10^{-4}	[-]	Volumetric expansion coefficient (salinity)
A_H	1.6×10^7	$[m^2s^{-1}]$	Horizontal mixing coefficient for momentum
A_V	1.0×10^{-3}	$[m^2s^{-1}]$	Vertical mixing coefficient for momentum
K_H	1.0×10^3	$[m^2s^{-1}]$	Horizontal mixing coefficient for heat and salt
K_V	8.0×10^{-5}	$[m^2s^{-1}]$	Vertical mixing coefficient for heat and salt
qz	1.8	[-]	Grid stretching
c_p	4.0×10^3	$[Jkg^{-1}K^{-1}]$	Specific heat capacity of seawater

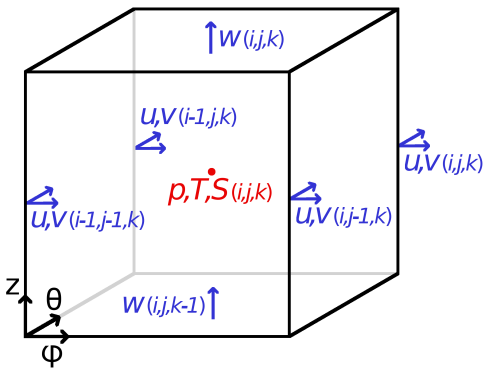

Figure 2.1: Schematic representation of a grid box at location ϕ_i, θ_j, z_k and variable positions near this grid box. The zonal and meridional velocities (respectively u, v, and w) are located at the middle of the grid edges, the vertical velocity (w) at the center of the top edge. Pressure, temperature and salinity (respectively p, T and S) are located at the center of the grid box.

of the six unknown variables u, v, w, p, T and S and a part (right hand side) that contains all other terms. The system can then be written as follows

$$\mathbf{B}\frac{\mathrm{d}\mathbf{u}}{\mathrm{d}t} = \mathbf{F}(\mathbf{u},\mathbf{q}). \tag{2.1}$$

The six unknown variables at each gridpoint are contained in the state vector $\mathbf{u} = (u, v, w, p, T, S)$ and thus has dimension $d = 6 \times N \times M \times L$, vector $\mathbf{q}$ contains an amount of q parameters (e.g. wind forcing strength, vertical Ekman number,...) and thus has dimension q, $\mathbf{B}$ is a linear operator (a $d \times d$ matrix that when acting on the time derivative of vector $\mathbf{u}$ gives a vector containing all time derivative terms of the system of equations) and $\mathbf{F}$ is a nonlinear operator mapping from $\mathbb{R}^{d+p} \rightarrow \mathbb{R}^d$ (when $\mathbf{F}$ acts on vectors $\mathbf{u}$ and $\mathbf{q}$ of dimension $d+q$ it returns a vector of dimension d containing all non-time derivative terms of the system of equations). The state vector $\mathbf{u}$ corresponds to the discretised solution of the system of equations in Equation 2.1 and is dependent on the parameters in vector $\mathbf{q}$.
When using timestepping methods, one would discretise the time derivative of $\mathbf{u}$ and compute a new solution for $\mathbf{u}$ after a step in time, starting with a known solution. The time integration can then be repeated until a steady state is reached. This can, however, only be done for one set of parameters q. To study the dependence of a steady state on a change in parameter, one thus has to repeat the time integration for each parameter value until steady state is reached.
With continuation methods, the steady state solution for a set of parameters is computed directly by solving

$$0 = \mathbf{F}(\mathbf{u},\mathbf{q}). \tag{2.2}$$

This allows for the direct computation of branches of steady state solutions as a function of one of the parameters in q, say μ, such that a bifurcation diagram can be constructed. The found steady state solutions can be stable, such as the steady states found through time integration, or unstable. To compute such a branch of steady state solutions, a pseudo-arclength method (Keller, 1977) is used. The idea of this method is to parameterise the branch(es) of solutions with an arclength parameter s, such that the branch is given by $\Gamma(s) = (\mu(s), \mathbf{u}(s))$. As the arclength parameter s introduces an extra unknown variable, an extra equation is obtained by "normalising" the tangent to branch $\Gamma(s)$. Starting from a known solution (known μ_0 and $\mathbf{u_0}$), the arclength parameter is changed with stepsize Δs and the new solution along the branch (new μ and $\mathbf{u}$) is calculated. The calculation of the new solution is done by solving the system of the equations in Equation 2.2 and the extra equation for arclength parameter s through iterative solvers. A more detailed explanation of how the system of equations is solved and which solvers are used can be found in de Niet et al. (2007) and Thies et al. (2009).

In an ocean model such as THCM, that directly solves for a steady state, it is possible to follow this steady state while smoothly changing the forcing field. To do so, a homotopy parameter is used. For example, to go from forcing field F_0 to forcing field F_1, a forcing field F_H that is a linear combination of both fields is defined using homotopy parameter α_H as follows

$$F_H(\alpha_H) = \alpha_H F_1 + (1-\alpha_H) F_0, \tag{2.3}$$

such that a value of $\alpha_H = 0$ corresponds to field F_0 and $\alpha_H = 1$ to field F_1. The field F_1 can be completely different or unrelated to F_0, though F_1 can also include a specific change with respect to F_0, such as a perturbation. In the latter case $F_1 = F_0 + F_{pert}$ gives the forcing field perturbed by perturbation F_{pert} and homotopy parameter α_H describes the perturbation strength.
This method is also used for finding the initial equilibrium solution (spinup). In this case the homotopy parameter describes the strength of e.g. salinity forcing in a continuation from a field with no forcing (F_0) to the full salinity forcing field (F_1).

2.1.2 Parametrisations and parameter choices

Horizontal mixing coefficient of momentum

Horizontal and vertical mixing of momentum, heat and salt is represented by eddy diffusion with mixing coefficients A_H, A_V for momentum and K_H, K_V for heat and salt. Typically, the values used for these coefficients are $A_H = 2.5 \times 10^5$ m^{2}s^{-1}, $A_V = 1.0 \times 10^{-3}$ m^{2}s^{-1}, $K_H = 1.0 \times 10^3$ m^{2}s^{-1} and $K_V = 8.0 \times 10^{-5}$ m^{2}s^{-1} (see e.g. de Niet et al. (2007)) With this value of A_H, however, the model did not succeed to continue to a global restoring equilibrium solution for all cases with non-idealised forcing and a paleobathymetry as described in section 2.2. When succeeding the computation time was significantly longer than with a higher value of A_H. For these reasons the horizontal mixing is increased to $A_H = 1.6 \times 10^7$ m^{2}s^{-1}.
This change mostly seems to impact the barotropic streamfunction, which is less detailed and much weaker than with a lower value of A_H. There seem to be some differences in the pattern of the meridional overturning streamfunction, for example the surface overturning cells seem to reach to greater depth with a lower value of A_H. The overturning strength and general MOC-pattern, however, appear to be the similar for both values of A_H.

Convective overturning

In order to solve convective processes, an extremely high model resolution is required, which is often not feasible. So, to represent convective overturning and hence to obtain stably stratified solutions in ocean models, often a convective adjustment scheme is used. This parametrisation induces a strong extra vertical mixing when the solution is unstably stratified and is turned off when the solution is stably stratified. The implicit nature of the model places a restriction on the use of convective adjustment to represent convective overturning. Using convective adjustment methods can lead to convergence problems or spurious equilibria (den Toom et al., 2011) can occur due to local on/off behaviour of vertical mixing depending on the vertical density gradient. Under restoring boundary conditions this behaviour was found to be relatively weak or absent and hence obtaining a restoring solution with convective adjustment was possible. Under mixed boundary conditions, however, many spurious bifurcations occur making it already very hard to obtain a bifurcation diagram for a smaller domain without land and bathymetry under idealised forcing. Moreover, as multiple equilibria are studied, the occurrence of artificial equilibria due to the way that convective adjustment is treated in the model is unwanted. For these reasons a convective adjustment scheme is not applied and the solutions are "pure" solutions of the governing system of equations. It is, however, possible for unstable stratifications to occur.
The absence of a convective adjustment scheme most clearly seems to impact the (global average) temperature, which is much higher without convective adjustment. Furthermore, the (global average) salinity is somewhat higher without the use of convective adjustment. The effect on the barotropic and overturning streamfunction is more indirect, hence the exact effect differs per case and can not be clearly predicted. A test with convective adjustment for 40 Ma resulted in the same overturning streamfunction pattern but with a higher overturning strength. The barotropic streamfunction in this case had the same pattern as well with a stronger circulation of the southern hemisphere cell.

As in the THCM simulations the horizontal mixing coefficient of momentum is set relatively large and convective adjustment was switched off (see above) we do not expect to reproduce all details of flow patterns and magnitude of variables as in other (more realistic) model studies. Many characteristics of the flow are, however, similar. Hence the focus of the solutions in the results will be mainly on the (changes in) pattern and relative magnitudes of variables.

2.1.3 Model diagnostics

For the further study of the obtained solutions of the model, a meridional overturning streamfunction, barotropic streamfunction and potential density are calculated. Several averages, a global, surface and zonal average, are defined as well. Furthermore, the meridional heat transport is calculated. The definition of these streamfunctions, averages and the meridional heat transport is given below as continuous functions for readability. In practice, a discrete version of these functions is used.

The Meridional Overturning Circulation (MOC) is represented in the solutions with a meridional overturning streamfunction ψ_o, which is calculated from meridional velocity v as follows

$$\psi_o(\theta,z) = -\int_{z=-D}^{z}\int_{\phi=\phi_W}^{\phi=\phi_E} v\left(\phi',\theta,z'\right)\,\cos\theta\,\mathrm{d}\phi'\,\mathrm{d}z', \tag{2.4}$$

where $D = 5000$ m is the ocean depth and ϕ_W and ϕ_E are the eastern and western boundary of the domain. For calculation of the global overturning streamfunction, $\phi_W = 0°$E and $\phi_E = 360°$E. When the overturning streamfunction is calculated for a separate basin, as defined in Figure 2.3 (see section 2.2), ϕ_W and ϕ_E are the eastern and western continental boundaries of that basin, dependent on latitude θ. The overturning streamfunction ψ_o is defined such that in a (θ,z)-plot it is positive for clockwise/northward surface circulation, negative for anticlockwise/southward surface circulation.

The barotropic streamfunction ψ_b is calculated from zonal velocity u as follows

$$\psi_b(\phi,\theta) = \int_{\theta}^{\theta=\theta_N}\int_{z=-D}^{z=0} u\left(\phi,\theta',z'\right)\,\mathrm{d}z'\,\mathrm{d}\theta', \tag{2.5}$$

where $z = 0$ is the surface and θ_N the northern boundary of the basin. It is defined such that a positive ψ_b corresponds to a clockwise circulation and a negative ψ_b to an anticlockwise circulation.

The global average $\bar{x}$ of a variable x (e.g. salinity, temperature) over basin volume V is defined as

$$\bar{x} = \frac{1}{|V|}\int_V x(\phi,\theta,z)\; r_0^2\cos\theta\,\mathrm{d}\phi\,\mathrm{d}\theta\,\mathrm{d}z, \tag{2.6}$$

where is assumed that $D \ll r_0$, r_0 is the earth's radius and $|V| = \int_V r_0^2\cos\theta\,\mathrm{d}\phi\,\mathrm{d}\theta\,\mathrm{d}z$ is the approximate total ocean volume.
Similarly, the upper layer "surface" average $\tilde{y}$ of a variable y (e.g. upper layer salinity) over basin surface S is defined as

$$\tilde{y} = \frac{1}{|S|}\int_S y(\phi,\theta)\; r_0^2\cos\theta\,\mathrm{d}\phi\,\mathrm{d}\theta, \tag{2.7}$$

where $|S| = \int_S r_0^2\cos\theta\,\mathrm{d}\phi\,\mathrm{d}\theta$ is the total ocean surface, and the zonal average $\hat{x}$ of a variable x (e.g. salinity, temperature) as

$$\hat{x}(\theta,z) = \frac{1}{|C|}\int_{\phi=\phi_W}^{\phi=\phi_E} x\left(\phi',\theta,z\right)\; r_0\cos\theta\,\mathrm{d}\phi', \tag{2.8}$$

where $|C| = \int_{\phi_W}^{\phi_E} r_0\cos\theta\,\mathrm{d}\phi$ is the part of the circumference of the earth in zonal direction at latitude θ that consists of ocean.

The meridional heat transport MHT is calculated from meridional velocity v and temperature T as follows

$$MHT(\theta) = c_p\rho_0\int_{z=-D}^{z=0}\int_{\phi=\phi_W}^{\phi=\phi_E} v\left(\phi',\theta,z'\right)\; T\left(\phi',\theta,z'\right)\,\cos\theta\,\mathrm{d}\phi'\,\mathrm{d}z', \tag{2.9}$$

where $c_p = 4.0\times10^3$ Jkg^{-1}K^{-1} is the specific heat capacity of seawater and $\rho_0 = 1.024\times10^3$ kgm^{-3} the reference density.

2.2 Paleobathymetry

Two different Late Eocene/Early Oligocene paleobathymetries, at 40 Ma and 30 Ma, are considered. These paleobathymetries are constructed as described in Mulder et al. (2017), section 3.1 and based on the reconstruction in Baatsen et al. (2016). For the model to be able to converge to a steady state solution and to reduce computing time, the Arctic ocean and inland seas are removed and the land-sea mask is smoothed. The resulting paleobathymetries at model resolution are shown in Figure 2.2. In both bathymetries the Southern Ocean gateways are open, though they are much narrower and shallower compared to the present-day bathymetry.
The oceans are subdivided into basins as shown in Figure 2.3. To be able to calculate an overturning streamfunction, each basin must be bordered by continents on the east and west side, hence some parts of the ocean spread across multiple basins. These parts of the ocean are left unassigned (white areas in Figure 2.3) as they consist of only a few latitudes. An exception is the part that covers both the Indian and Pacific Ocean as it consists of a larger ocean area, especially in the 40 Ma paleobathymetry. This part is defined as its own basin, the Indian/Pacific (teal areas in Figure 2.3).
The general continental configuration is relatively similar for both bathymetries, however, there are some subtle differences. In the 30 Ma bathymetry with respect to the 40 Ma bathymetry, Australia has moved northward as the Tasman gateway widens and becomes deeper and the ocean between Australia and South-East Asia becomes shallower. Furthermore, both North and South America have moved to the northwest, widening the Atlantic ocean and narrowing the Pacific ocean. Africa has moved slightly northward, narrowing the Tethys sea, and India moved northward, connecting to the Eurasian continent.

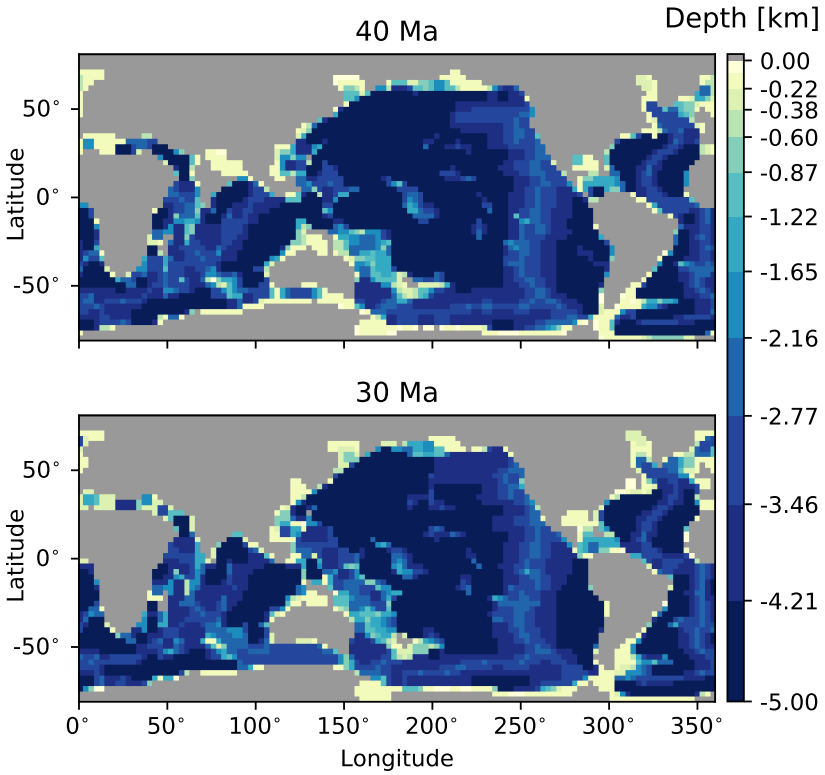

Figure 2.2: Paleobathymetries for 40 Ma and 30 Ma at model resolution (3° in horizontal direction, 12 vertical levels), based on the reconstruction in Baatsen et al. (2016). The twelve non-equidistant depth levels are indicated by colours, grey indicates land. The depth tick label at the first layer as seen from the surface (−0.095 km) is removed for readability.

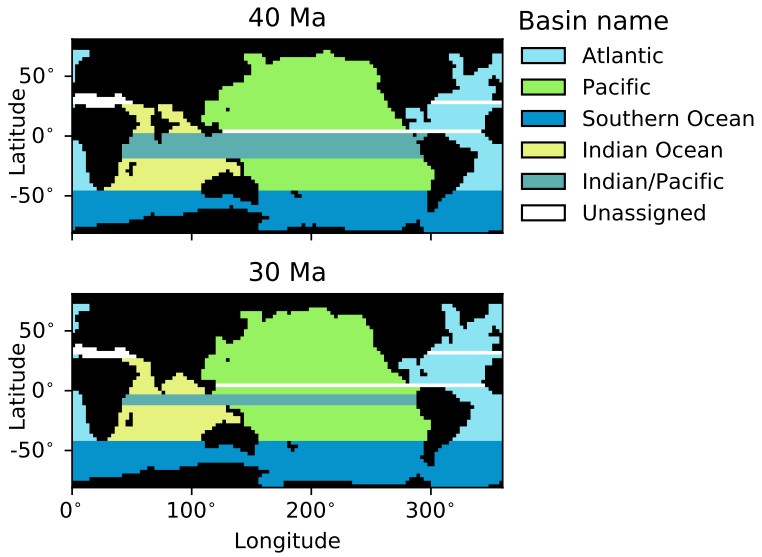

Figure 2.3: Division of oceans into basins, each basin is indicated by a colour, as indicated in the legend, for 40 Ma and 30 Ma. The basins are bounded by continents on the east and west side to be able to calculate an overturning streamfunction in each basin. The white areas spread across multiple basins and are left unassigned.

2.3 Surface forcing

As described in section 2.1, the ocean model is forced at the upper layer with prescribed fields for wind stress, upper layer temperature and, in case of restoring boundary conditions, upper layer salinity. In order to obtain a relatively "realistic" surface forcing, these fields are taken from equilibrium ocean circulation states at 38 Ma and 30 Ma, obtained with the Community Earth System Model (CESM) in Baatsen (2019); Baatsen et al. (2020). Technically these ocean circulation states are not exactly in equilibrium as they are obtained using time integration. They have, however, been integrated for 3000-4000 years and are considered to be close enough to an equilibrium state to treat as such. Hence the CESM ocean circulation states will be referred to as equilibrium solutions, with the last 50 model years used as a representative of the equilibrium climate. For the temperature and salinity forcing the depth-average temperature and salinity of the upper 100 m from the CESM equilibrium state are used, as this is similar to the depth of the upper layer in the model (95 m). For wind stress forcing the wind stress at the ocean surface is used. The forcing fields for the 40 Ma paleobathymetry simulations are taken from the 38 Ma equilibrium state under 4× pre-industrial CO_2 forcing (38 Ma 4PIC), the forcing fields for the 30 Ma simulations are taken from the 30 Ma equilibrium state under 2× pre-industrial CO_2 forcing (30 Ma 2PIC). To study the influence of paleobathymetry and CO_2 forcing separately, an extra simulation is performed for the 40 Ma paleobathymetry with the forcing fields taken from the 38 Ma CESM equilibrium state under 2× pre-industrial CO_2 forcing (38 Ma 2PIC). Even though the CESM simulations are obtained using both Late Eocene and Early Oligocene bathymetries, no Antarctic ice sheet is present in these simulations, which makes the forcing fields more representative of a Late Eocene climate.
As the simulations in Baatsen (2019) are performed on a curvilinear grid, the wind stress, temperature and salinity fields are interpolated to a rectangular grid with a resolution of 1° to obtain the grid needed for forcing input. When the forcing fields are inserted in the model, they are downscaled to the model resolution of 3° and ocean points with no forcing data are interpolated. The latter is needed because there are some small differences between in continental geometry of the CESM simulations and the continental geometry as used in this study (see section 2.2). The resulting forcing fields for 38 Ma 4PIC and 30 Ma 2PIC are shown in respectively Figure 2.4 and Figure 2.5. The forcing fields for 38 Ma 2PIC are not shown as they are relatively similar the 30 Ma 2PIC forcing fields,

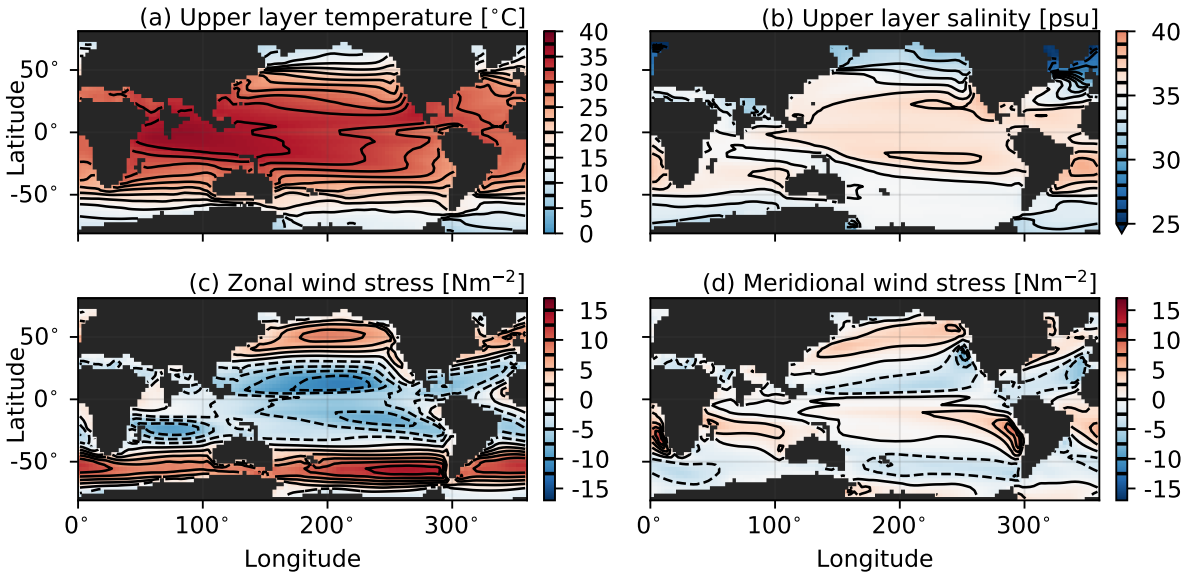

Figure 2.4: Plots of upper layer forcing after downscaling and interpolation from the CESM 38 Ma equilibrium ocean circulation state under 4× pre-industrial CO_2 forcing from Baatsen (2019); (a) upper layer temperature, (b) upper layer salinity, (c) zonal wind stress and (d) meridional wind stress. Upper layer temperature and salinity are depth-averaged values over the first 100 m of the CESM equilibrium state. The global average upper layer temperature is 27.4 °C, the global average upper layer salinity is 35.4 psu. Contours are drawn at an interval of respectively 2.5 °C, 1 psu and 2.5 Nm^{-2} and are indicated on the colorbar.

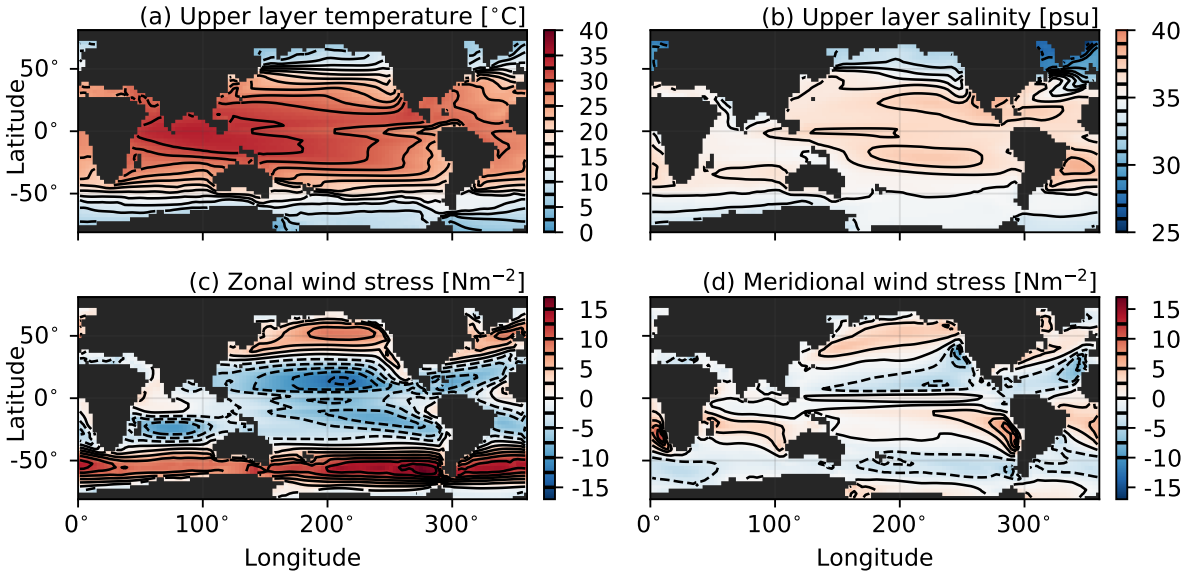

Figure 2.5: Plots of upper layer forcing after downscaling and interpolation from the CESM 30 Ma equilibrium ocean circulation state under 2× pre-industrial CO_2 forcing from Baatsen (2019); (a) upper layer temperature, (b) upper layer salinity, (c) zonal wind stress and (d) meridional wind stress. Upper layer temperature and salinity are depth-averaged values over the first 100 m of the CESM equilibrium state. The global average upper layer temperature is 24.5 °C, the global average upper layer salinity is 35.7 psu.

with a global average upper layer temperature of 25.0 °C, a global average upper layer salinity of 35.4 psu and a zonal average zonal wind stress at 57°S of 11.3 Nm^{-2}.
The upper layer salinity forcing in the northernmost part of the Atlantic is notably much fresher than other parts of the ocean. This is a result of the Arctic ocean being very isolated and therefore very fresh in the CESM simulation. Even though the Arctic is absent in our simulations, this effect is still present in the forcing. As the very northernmost part of the Atlantic, north of 54°N, is relatively shallow and separated to the rest of the Atlantic basin by a small ridge, the water in this part is consequently much fresher than in the rest of the basin.
The largest difference between the 38 Ma 4PIC and 30 Ma 2PIC forcing is in the global average upper layer temperature, which is almost three degrees higher for the 38 Ma 4PIC forcing (27.4 °C versus 24.5 °C). Global average upper layer salinity is 0.3 psu higher for the 30 Ma 2PIC forcing (35.7 psu versus 35.4 psu). The spatial pattern upper layer temperature and salinity is relatively similar for both forcings, as is the spatial pattern in zonal and meridional wind stress. The magnitude of the extrema in zonal wind stress though, is somewhat larger for the 30 Ma 2PIC forcing. Especially the maximum in zonal wind stress west of the tip of the South American continent, which is 3.1 Nm^{-2} larger in the 30 Ma 2PIC forcing. The zonal average zonal wind stress at this latitude is larger for the 30 Ma 2PIC forcing as well, with a value of 11.8 Nm^{-2} compared to 10.4 Nm^{-2} at 57°S.
For both 38 Ma 4PIC and 30 Ma 2PIC forcing there is a north-south asymmetry for upper layer temperature and salinity, which is possibly linked to both CESM simulations having a southern sinking equilibrium ocean circulation state. The zonal average upper layer temperature in the northern hemisphere is lower than at the same latitude in the southern hemisphere. At a latitude of 60° this difference is 2.5 °C (3.1 °C) for 38 Ma 4PIC (30 Ma 2PIC) forcing. Similarly, the zonal average upper layer salinity above 15° (27°) latitude is lower for the northern hemisphere than for the southern hemisphere, with a difference of 3.3 psu (3.1 psu) at 60° latitude for 38 Ma 4PIC (30 Ma 2PIC) forcing.

2.3.1 Modified surface forcing

In order to study the effect of the north-south asymmetry in salinity forcing on the meridional overturning circulation, simulations where the salinity forcing is mirrored at the equator were performed. As mirroring the full upper layer salinity field in the equator would result in a misalignment of the spatial pattern with continental boundaries and a large amount of points that need to be interpolated, the zonal average of the field is mirrored instead. Additionally, to reduce the north-south asymmetry of the temperature forcing, the upper layer temperature field is modified such that its zonal average is symmetric around the equator.
The modified forcing fields are constructed from the upper layer temperature and salinity fields for 38 Ma 4PIC and 30 Ma 2PIC that are downscaled and interpolated to a rectangular 1° grid. Before a zonal average is calculated, the field is masked to exclude inland seas and the Arctic sea as these are present in the continental geometry of the CESM simulations but not included in our bathymetry (see section 2.2). Data from high northern latitudes with few ocean gridpoints is excluded as well to prevent a sudden drop in zonal average upper layer salinity towards the north, caused by the low salinity in the North Atlantic. All ocean points at a certain latitude are assumed to have the same zonal average value to create a forcing field.
The mirrored zonal average salinity forcing is constructed by mirroring the zonal average upper layer salinity field in the equator. As the southern part of the ocean basin reaches to higher latitudes than the northern part, the mirrored zonal average upper layer salinity field has no data for the southernmost latitudes. These missing values are filled by a linear extrapolation based on the slope in zonal average upper layer salinity south of 15°S.
To symmetrise the upper layer temperature field, its zonal average is made symmetric around the equator. The zonal average upper layer temperature is calculated after excluding the same points from the field as for the calculation of zonal average upper layer salinity. For each latitude the difference between the zonal average upper layer temperature and the mean of the zonal average upper

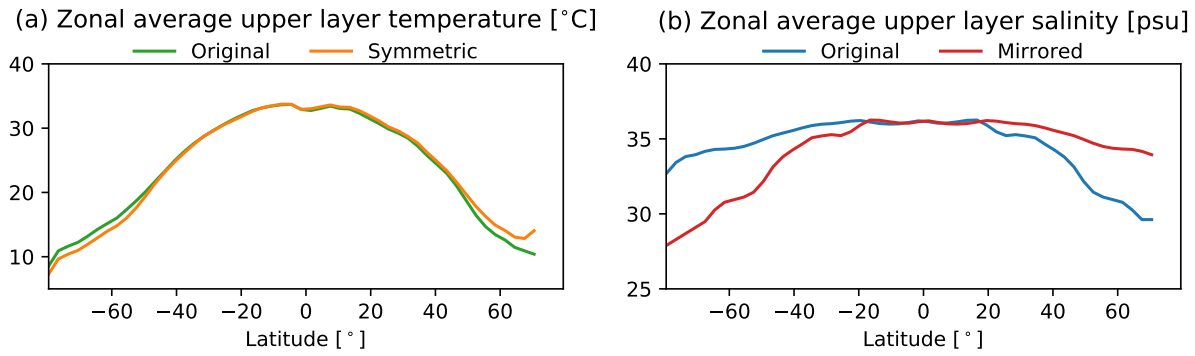

Figure 2.6: Plots of (modified) zonal average upper layer forcing for the 38 Ma 4PIC case; (a) unmodified (original) zonal average upper layer temperature (same as in Figure 2.4) and zonal average upper layer temperature after it is made symmetric and (b) unmodified (original) zonal average upper layer salinity and mirrored zonal average upper layer salinity.

layer temperature at that latitude in the northern and southern hemisphere is calculated. The upper layer temperature field is then corrected with this difference. For the high latitudes at the southern hemisphere where no zonal average value is available at the equivalent latitude in the northern hemisphere and hence no mean can be calculated, the correction at the highest latitude where there is a zonal average value available at the northern hemisphere, is used instead. Finally, the field is corrected such that the surface average upper layer temperature is the same as before the field is made symmetric.
When the resulting modified forcing fields, the zonal average upper layer salinity, mirrored zonal average upper layer salinity and symmetrised upper layer temperature for 38 Ma 4PIC and 30 Ma 2PIC, are inserted into the model, they are downscaled to the model resolution of 3° and missing points are interpolated. Because of this, the zonal average of the symmetrised upper layer temperature field is not exactly symmetric around the equator, though it is much more symmetric than the original upper layer temperature field. The zonal average upper layer temperature as it is originally and after it is made symmetric are shown in Figure 2.6a, the zonal average upper layer salinity as it is originally and after it is mirrored in the equator are shown in Figure 2.6b. As is visible in this figure, the difference between the original and symmetric upper layer temperature fields is quite small, hence the symmetric upper layer temperature forcing fields look quite similar to the ones shown in Figure 2.4 and Figure 2.5. As the modified upper layer salinity forcing uses a zonal average profile, the resulting forcing fields have no east-west variations. The global average upper layer temperature is 27.4 °C for both the original and symmetric temperature fields, the global average upper layer salinity is 35.3 psu for the original forcing and 34.9 psu for the mirrored forcing. This difference in global average upper layer salinity is due to the larger area of ocean at high latitudes in the southern hemisphere compared to the northern hemisphere.

2.4 Equation of State

One of the governing equations in the model is the equation of state, that gives the dependence of density (ρ) on temperature (T) and salinity (S). The model is executed with a linear equation of state that is defined as

$$\rho = \rho_0 (1 - \alpha_T (T - T_0) + \alpha_S (S - S_0)). \tag{2.10}$$

Here $\rho_0 = 1.024 \times 10^3$ kgm^{-3}, $T_0 = 15$ °C and $S_0 = 35$ psu are respectively the reference density, reference temperature and reference salinity. The volumetric expansion coefficients for temperature and salinity, α_T and α_S, are usually taken to have the values of $\alpha_T = 1.0 \times 10^{-4}$ K^{-1} and $\alpha_S = 7.6 \times 10^{-4}$ psu^{-1} (Dijkstra, 2008).

For a present-day climate the linear equation of state with these conventional values of α_T and α_S gives a relatively good approximation to a more accurate equation of state (e.g. Gill (1982)). In the warmer paleo climate for 40 Ma and 30 Ma, however, the density obtained with this linear equation of state with conventional values for α_T and α_S gives a too strong dependency on salinity (see Figure 2.7). Consequently, when calculating the upper layer density from the CESM upper layer temperature and salinity (see section 2.3) with this present-day linear equation of state, the result (linear present) differs quite a bit from the upper layer density directly obtained from the CESM simulation (CESM) or when using the nonlinear equation of state from Gill (1982) (nonlinear), as shown in Figure 2.8. The spatial pattern of upper layer density for the present-day linear equation of state corresponds more to the spatial pattern of upper layer salinity, while for the upper layer density from the CESM simulation and calculated with the nonlinear equation of state the spatial pattern corresponds more to that of upper layer temperature. Furthermore, the location with highest upper layer density is in the South Atlantic for the present-day linear equation of state, while it is in the Southern Ocean for the CESM simulation and nonlinear equation of state.
To obtain values for the volumetric expansion coefficients that are suitable for the warmer climate at 40 Ma and 30 Ma, α_T and α_S are determined by a least squares fit to the nonlinear equation of state in Gill (1982). This is done for a range of temperatures of 0 °C to 40 °C and range of salinities of 20 psu to 40 psu. A plot of density as a function of temperature and salinity according to the nonlinear equation of state from Gill (1982) (colours) and the fitted linear equation of state with values of $\alpha_T = 2.16 \times 10^{-4}$ K^{-1} and $\alpha_s = 6.42 \times 10^{-4}$ psu^{-1} (solid lines) is given in Figure 2.7. The density for the linear equation of state with more conventional values of $\alpha_T = 1.0 \times 10^{-4}$ K^{-1} and $\alpha_S = 7.6 \times 10^{-4}$ psu^{-1} is shown as well (dotted lines). It is visible that the linear equation of state with fitted α_T and α_S still tends to overestimate the density for most combinations of temperature and salinity, especially for relatively high temperatures and/or relatively low salinities. For relatively high salinities and relatively neutral to low temperatures it tends to underestimate the density. Over/underestimation of the density is, however, something that will always occur to some extent when a linear equation of state is used.
The upper layer density calculated using the linear equation of state with α_T and α_S adapted to the paleo climate (linear paleo) is shown in Figure 2.8. The spatial pattern of this upper layer density is much more similar to that of the CESM simulation and for nonlinear equation of state than that for the linear equation of state with present-day coefficients. It also follows the same spatial pattern as the upper layer temperature and the location of highest density is in the Southern Ocean.
A simulation was performed for 40 Ma using either the present-day or adapted values for α_T and α_S and restoring forcing using the 38 Ma 4PIC upper layer/surface fields as described in section 2.3. After a continuation to full forcing, the steady state MOC found with the present-day volumetric expansion coefficients was a circulation with sinking at the equator. For the adapted volumetric expansion coefficients the found steady state had a southern sinking MOC solution, which corresponds to the MOC state in the CESM simulation the forcing was taken from.
As both the MOC state and the spatial pattern in upper layer density obtained with the linear equation of state with adapted α_T and α_S correspond relatively well to those of the CESM simulation, definitely much better than for the linear equation of state with present-day α_T and α_S, it is assumed that the linear equation of state with adapted α_T and α_S gives a good enough approximation of the full equation of state to obtain sufficiently accurate enough steady state solutions.

To account for the effects of pressure on temperature, and consequently density, at greater depths, potential density is calculated and used for the simulation results. First potential temperature is calculated from temperature, salinity and pressure as given in Gill (1982), where pressure is assumed to be purely hydrostatic, thus $p(z) = -\rho_0 g z$, where $\rho_0 = 1.024 \times 10^3$ kgm^{-3} is the reference density and $g = 9.8$ ms^{-2} the standard acceleration due to gravity. Then potential temperature is used instead of temperature in the equation of state (see Equation 2.10) to calculate the potential density.

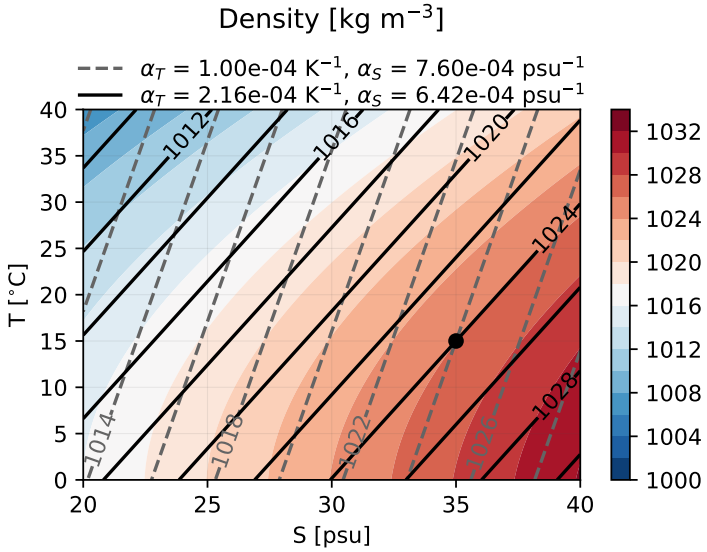

Figure 2.7: A plot of density as a function of temperature (T) and salinity (S) for the nonlinear equation of state as given in Gill (1982) (colours), for the linear equation of state with conventional volumetric expansion coefficients (dashed lines) and for the linear equation of state with fitted volumetric expansion coefficients (solid lines). The dot indicates the reference density at reference temperature and salinity for the linear equation of state.

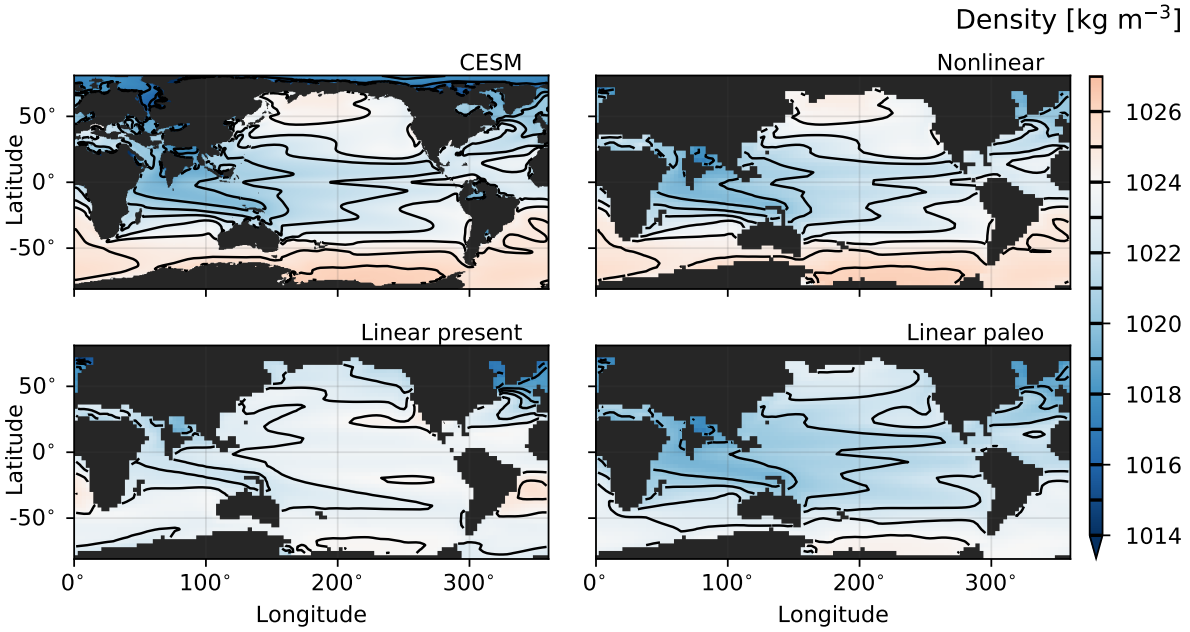

Figure 2.8: Plots of upper layer density for 38 Ma 4PIC (CESM) found for the equilibrium state in Baatsen (2019) and calculated from the CESM upper layer temperature and salinity (see Figure 2.4) using (nonlinear) a nonlinear equation of state as given in Gill (1982), (linear present) a linear equation of state with conventional present-day volumetric expansion coefficients $\alpha_T = 1.0 \times 10^{-4}$ K^{-1} and $\alpha_S = 7.6 \times 10^{-4}$ psu^{-1} and (linear paleo) a linear equation of state with volumetric expansion coefficients adapted for a paleo climate $\alpha_T = 2.16 \times 10^{-4}$ K^{-1} and $\alpha_s = 6.42 \times 10^{-4}$ psu^{-1}. Contours are drawn at an interval of 1 kg m^{-3} and are indicated on the colorbar.

3 Results

3.1 Steady states under restoring boundary conditions

A steady state solution under restoring boundary conditions is obtained by starting with a trivial, no flow and homogeneous, solution without upper layer wind stress, temperature and salinity forcing. Using the continuation methods as described in subsection 2.1.1 the forcing strength is increased until full forcing is reached. From this solution a freshwater flux is diagnosed and barotropic streamfunction, meridional overturning streamfunction, zonal average potential density and zonal average temperature and salinity are calculated (see subsection 2.1.3 for definitions). The upper layer temperature and salinity for the restoring steady state solution are very similar to the forcing, with only small differences due to the restoring timescale. To indicate the overturning strength, the minimum and maximum in meridional overturning streamfunction (from now on referred to as overturning streamfunction) are calculated for below 500 m depth. This is done to exclude the small but strong overturning cells near the surface that are a result of the wind-driven circulation.
The steady state solutions found for the two different paleobathymetries (see section 2.2) under two different CO_2 forcings (see section 2.3) are given below. To distinguish between the effect of bathymetry and the effect of CO_2 forcing, a short description of a third steady state solution for 40 Ma paleobathymetry with 38Ma 2PIC forcing is included. The results are compared with the CESM equilibrium solutions from Baatsen (2019) where the temperature, salinity and wind stress fields used as forcing are taken from. Values for the minimum and maximum of the overturning streamfunction, the minimum and maximum of the barotropic streamfunction, and the minimum and maximum of the zonal average diagnosed freshwater flux of each solution are given in Table 3.1 and the average temperature and average salinity, globally, upper 1000 m, below 2000 m and per basin of each solution are given in Table 3.2. Figures of the overturning streamfunction per basin can be found in Appendix A for all of the solutions, indicated with the same letters as in Table 3.1 and Table 3.2, values of the minimum and maximum of the overturning streamfunction per basin are given above each of the subfigures.

3.1.1 40 Ma bathymetry, with 4× pre-industrial greenhouse gas levels

The results for the restoring steady state solution found for the 40 Ma paleobathymetry under 38Ma 4PIC forcing are shown in Figure 3.1, values are given in Table 3.1 and Table 3.2, indicated with 40 Ma R. A strong southern sinking MOC-state is found that consists of one large negative overturning cell. A negative overturning occurs in all basins and is strongest in the Southern Ocean and weakest in the Atlantic. The barotropic streamfunction consists of two main circulation cells, roughly corresponding to subtropical gyres, that are located in the North and South Pacific. Of these two cells the southern cell is largest and strongest. Western intensification is only slightly present and no clear boundary current can be distinguished. This is probably due to the large horizontal mixing coefficient for momentum that is taken (see subsection 2.1.2). Furthermore there is no clear presence of an Antarctic Circumpolar Current (ACC).
The global average ocean temperature is quite high, especially in the upper 1000m, which is a result of the absence of a convective adjustment scheme (see subsection 2.1.2). Global average salinity is highest in the upper 1000m. Compared to the other basins, the Atlantic has a higher average temperature and average salinity, the temperature is less stratified in the Atlantic as well. The spatial pattern in zonal average potential density is similar to the spatial pattern in zonal average temperature. A stratification is present, though in the southern high latitudes, the same latitudes as where deep water formation occurs, this stratification is unstable. In the northernmost part of the basin

Table 3.1: Values for the minimum and maximum of the overturning streamfunction below 500 m depth (OS min/max, values per basin can be found in the figures in Appendix A), the minimum and maximum of the barotropic streamfunction (BS min/max) and the minimum and maximum of the zonal average diagnosed freshwater flux (FF min/max, only for restoring solutions) for the restoring solutions for 40 Ma and 30 Ma as described in section 3.1 (R, R2 is the 40 Ma 2PIC solution) and the solutions in the bifurcation diagram for 40 Ma and 30 Ma, as shown in Figure 3.7 and Figure 3.8 (letters correspond to letters in figures).

	OS [Sv]		**BS [Sv]**		**FF [10^{-7}ms^{-1}]**	
	min	max	min	max	min	max
40 Ma R	-39.3	0.1	-25.1	16.8	-1.67	0.39
40 Ma R2	-49.5	1.5	-24.9	17.6	-1.47	0.37
30 Ma R	-50.7	2.2	-27.9	14.0	-1.50	0.35
40 Ma A	0.0	35.2	-12.9	25.8	-1.53	0.86
40 Ma B	-20.7	25.3	-13.3	24.1	-	-
40 Ma C	-30.0	6.4	-12.4	16.5	-	-
40 Ma D	-29.9	6.8	-32.8	15.9	-	-
40 Ma E	-45.8	3.5	-21.5	18.2	-1.07	0.47
30 Ma A	-0.1	37.5	-14.1	26.2	-1.43	1.01
30 Ma B	-12.0	17.2	-13.4	20.1	-	-
30 Ma C	-25.9	15.2	-14.5	23.0	-	-
30 Ma D	-33.4	8.7	-31.4	14.7	-	-
30 Ma E	-36.9	7.8	-30.9	14.6	-	-
30 Ma F	-47.4	0.4	-30.8	15.1	-1.17	0.41

Table 3.2: Values for temperature and salinity, the global average (G), average of the upper 1000 m (U), average below 2000 m (B) and per basin: Atlantic (Atl), Pacific (Pac), Indian Ocean (Ind) and Southern Ocean (SO) for the restoring solutions for 40 Ma and 30 Ma as described in section 3.1 (R, R2 is the 40 Ma 2PIC solution) and the solutions in the bifurcation diagram for 40 Ma and 30 Ma, as shown in Figure 3.7 and Figure 3.8 (letters correspond to letters in figures).

	Temperature [°C]							**Salinity [psu]**						
	Glob	U	B	Atl	Pac	Ind	SO	Glob	U	B	Atl	Pac	Ind	SO
40 Ma R	21.1	25.0	19.5	23.4	20.9	20.8	19.7	35.2	35.5	35.1	36.1	35.1	35.0	35.0
40 Ma R2	17.6	22.0	15.9	17.2	17.8	17.6	16.6	35.1	35.4	34.9	35.1	35.1	35.0	35.0
30 Ma R	17.3	21.8	15.7	16.7	17.7	17.2	16.4	35.2	35.7	35.1	35.2	35.3	35.1	35.1
40 Ma A	24.2	26.3	23.4	24.6	24.3	24.6	23.1	35.3	35.1	35.3	35.4	35.4	35.2	34.8
40 Ma B	22.1	25.4	20.8	20.1	23.3	20.9	20.5	34.8	35.0	34.7	34.2	35.2	34.3	34.4
40 Ma C	21.4	25.3	19.8	21.1	21.6	21.6	20.4	34.8	34.9	34.8	35.1	34.7	34.9	34.7
40 Ma D	22.3	25.6	20.8	24.8	21.8	22.5	21.1	35.3	35.4	35.2	36.0	35.2	35.1	34.9
40 Ma E	19.5	24.2	17.6	18.1	20.0	20.0	18.3	34.8	35.2	34.7	34.7	34.8	34.9	34.8
30 Ma A	20.5	23.1	19.5	20.5	20.6	21.4	19.5	35.5	35.5	35.5	35.6	35.6	35.5	35.1
30 Ma B	19.4	22.4	18.2	20.2	20.1	17.7	17.6	35.5	35.7	35.4	36.8	35.2	35.5	35.2
30 Ma C	18.4	22.0	17.0	15.9	19.9	16.6	16.9	35.5	35.7	35.4	35.5	35.5	35.5	35.4
30 Ma D	18.0	21.8	16.7	20.0	17.0	20.1	17.3	35.5	35.7	35.4	36.3	35.1	36.0	35.4
30 Ma E	17.6	21.6	16.2	19.2	17.3	18.5	16.4	35.5	35.8	35.4	36.1	35.4	35.5	35.2
30 Ma F	16.1	21.0	14.3	14.5	17.0	15.7	14.9	35.0	35.5	34.8	34.9	35.1	35.1	35.0

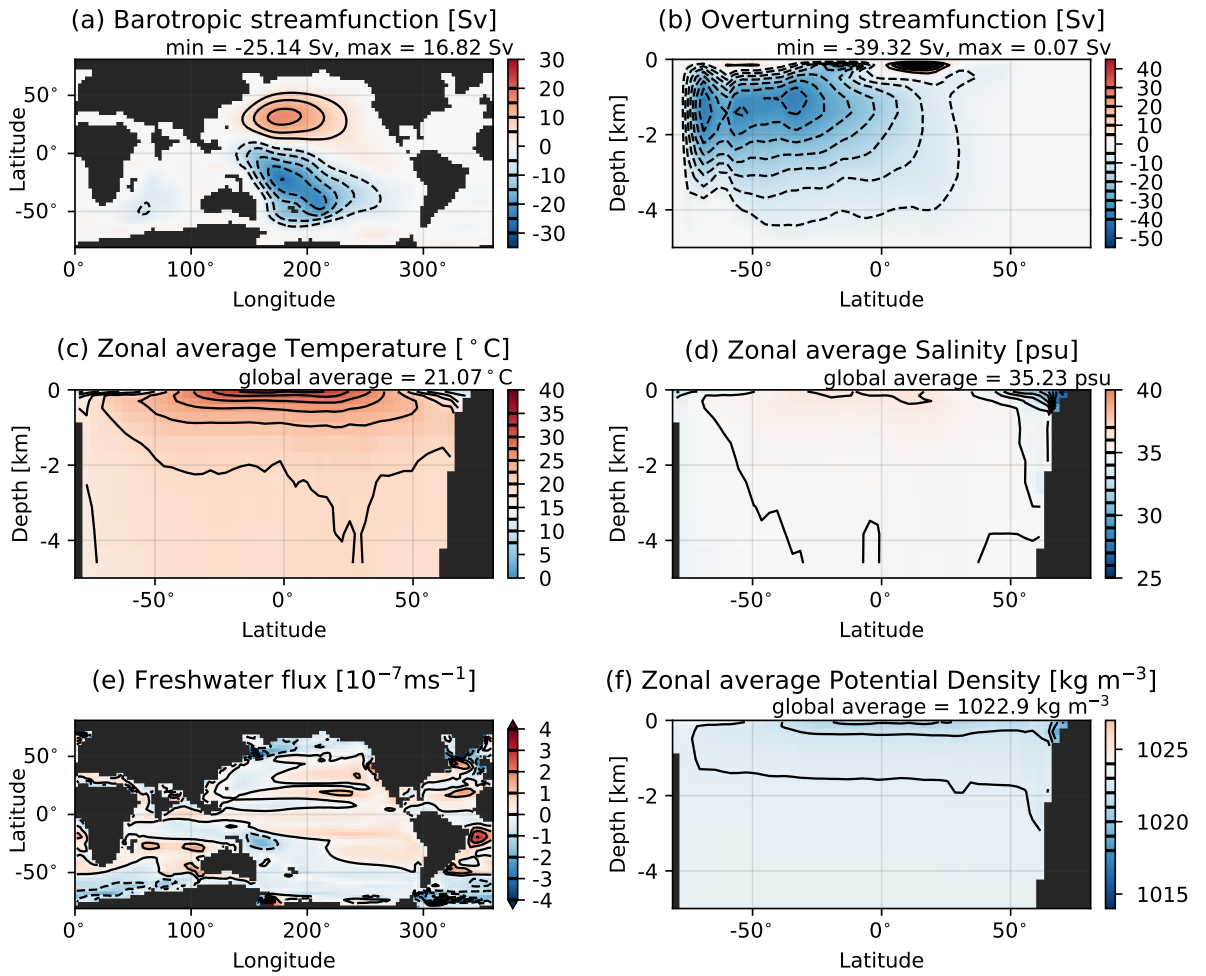

Figure 3.1: Plots of (a) barotropic streamfunction, (b) meridional overturning streamfunction, (c) zonal average temperature, (d) zonal average salinity, (e) diagnosed freshwater flux and (f) zonal average potential density for the restoring steady state solution for 40 Ma bathymetry under 38Ma 4PIC forcing. The minimum and maximum of the overturning streamfunction are calculated below a depth of 500 m. Contours are drawn at an interval of respectively 5 Sv, 2.5 °C, 1 psu, 10^{-7} ms^{-1} and 0.5 kgm^{-3} and are indicated on the colorbar.

there are locations where the stratification is unstable as well. The northernmost part of the Atlantic, north of 54°N, is colder, much fresher and consequently has a lower potential density compared to the rest of the Atlantic basin. This is a result of this northernmost part being relatively isolated in combination with the forcing (see section 2.3).
The magnitude of the diagnosed freshwater flux mostly stays within 10^{-7} ms^{-1}, with some peaks that have an amplitude of up to about 4×10^{-7} ms^{-1}. Even greater magnitudes occur where a positive and negative peak are located next to each other, such as in the Southern Ocean at about 165° longitude. This is, however, a result of a strong gradient in salinity between gridboxes in the forcing field that is smoothed out in the restoring solution and thus is considered unrealistic. The zonal average of the diagnosed freshwater is mostly positive between 49°S and 46°N and negative at the higher latitudes.

Comparison with CESM solution

The CESM equilibrium solution for 38 Ma paleobathymetry and 4PIC forcing has a southern sinking MOC-state as well, though the overturning strength found in the restoring solution is more than twice as strong as that of the CESM equilibrium. The minimum in overturning streamfunction is located at a somewhat shallower depth than in the CESM equilibrium, namely around 1.5 km depth instead of

around 2 km depth. Furthermore, the surface overturning cells, especially the one at around 55°S, are weaker and shallower than in the CESM equilibrium.
The two circulation cells in barotropic streamfunction in the Pacific, that roughly correspond to subtropical gyres, are also present in the CESM equilibrium solution. Here they are the largest positive and negative cell as well, and for both solutions the southern cell is strongest. In the CESM equilibrium, however, the two Pacific subtropical gyres are separated by small tropical circulation cells and other subtropical and subpolar gyres are present in the Indian, (South) Atlantic and Southern Ocean that have a similar magnitude to the Pacific subtropical gyres. The strongest positive circulation cell in the CESM solution is found in the South Atlantic/Southern Ocean and is not the North Pacific subtropical gyre, even though the North Pacific gyre is the largest positive cell in terms of size. In the CESM equilibrium a weak ACC is present that has a similar magnitude as the North Pacific cell, while in the restoring solution no ACC is present. Furthermore, the magnitude of the barotropic streamfunction of the restoring solution is much weaker, about a half of that of the CESM equilibrium.
The global average temperature is very high, almost 8 °C higher than in the CESM equilibrium solution (about 8.5 °C higher below 2000 m depth and is almost 6 °C higher for the upper 1000 m).
The diagnosed freshwater flux has a similar order of magnitude of $\sim 10^{-7}$ ms^{-1} and a similar spatial pattern as the freshwater flux of the CESM equilibrium solution. The diagnosed freshwater flux of the restoring solution, however, has quite a few peaks with an amplitude higher than 10^{-7} ms^{-1}, whereas the freshwater flux of the CESM equilibrium is much more smooth and mostly stays within an amplitude of 10^{-7} ms^{-1}.

3.1.2 30 Ma bathymetry, with $2\times$ pre-industrial greenhouse gas levels

The results for the restoring steady state solution found for the 30 Ma paleobathymetry under 30Ma 2PIC forcing are shown in Figure 3.2, values are given in Table 3.1 and Table 3.2, indicated with 30 Ma R. The MOC-state found in this case is a southern sinking solution that is even stronger than that of the 40 Ma 4PIC restoring solution, with a minimum of -50.7 Sv in the Southern Ocean. The overturning strength in the Pacific and Atlantic is about the same and is weaker for the Indian Ocean compared to the 40 Ma solution. Again, the barotropic streamfunction consists of two main circulation cells corresponding to subtropical gyres located in the North and South Pacific, with a southern cell that is larger and stronger and no clear presence of an ACC. Compared to the 40 Ma solution the South Pacific cell and small cells in the Indian Ocean and South Atlantic are somewhat stronger and the North Pacific cell somewhat weaker.
The global average temperature is 3.8 °C lower than that of the 40 Ma 4PIC restoring solution, while the difference in upper layer temperature forcing is only 2.9 °C. Especially the temperature below 2000 m depth is much cooler, with the same temperature difference as for the global average temperature. The coolest basin is again the Southern Ocean. Different to in the 40 Ma solution, the basin with the highest temperature is the Pacific. Global average salinity and average below 2000 m depth are the same as in the 40 Ma solution, though the upper 1000 m salinity and salinity per basin is a little higher. Just as for the 40 Ma solution, a stratification is present which is unstable in the southern high latitudes and at a few locations in the northernmost high latitudes. The unstable stratification in the northernmost part of the basin seems to be more strongly present than in the 40 Ma solution. The northernmost part of the Atlantic is still colder and fresher and consequently has a lower potential density than the rest of the Atlantic basin, though there is less of a difference than in the 40 Ma solution.
The spatial pattern of the diagnosed freshwater flux is very similar to that of the 40 Ma 4PIC restoring solution, the magnitude stays within 10^{-7} ms^{-1} as well. The magnitude and exact location of the peaks, however, differs somewhat. The peaks have an amplitude of up to about 5×10^{-7} ms^{-1}. The zonal average of the diagnosed freshwater flux is mostly positive between 46°S and 46°N, mostly negative at the higher latitudes.

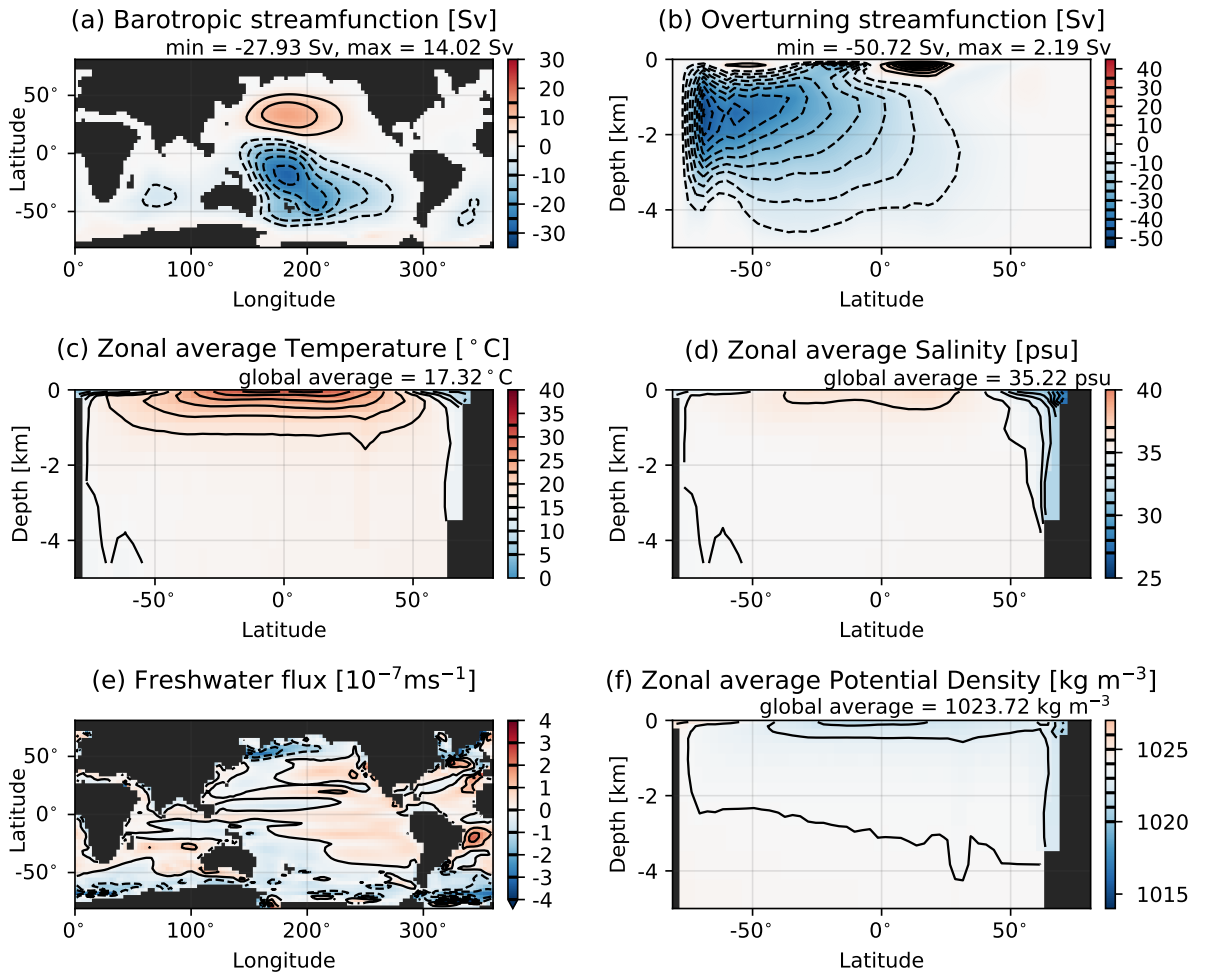

Figure 3.2: Plots of (a) barotropic streamfunction, (b) meridional overturning streamfunction, (c) zonal average temperature, (d) zonal average salinity, (e) diagnosed freshwater flux and (f) zonal average potential density for the restoring steady state solution for 30 Ma bathymetry under 30Ma 2PIC forcing. The minimum and maximum of the overturning streamfunction are calculated below a depth of 500 m.

Comparison with CESM solution

The CESM equilibrium solution for 30 Ma paleobathymetry and 2PIC forcing has a southern sinking MOC-state as well, though negative overturning mostly occurs below 2 km depth or in the Southern Ocean. Furthermore, in the CESM solution a weak positive overturning cell is present near the equator at about 1 km depth and the positive surface overturning cell at around 55°S reaches a depth of about 3.5 km. This spatial pattern in overturning is quite different to the one found in the restoring solution, where there is one strong negative overturning cell and the surface cells are much shallower. The minimum in overturning below 500 m depth of the restoring solution is more than twice as strong as the minimum in the CESM solution, which is similar to the difference for the 40 Ma 4PIC case. The minimum in overturning in both the restoring and CESM solution is located in the Southern Ocean and is stronger than in the 40 Ma 4PIC restoring and CESM solution respectively. The depth of the minimum in overturning is again shallower in the restoring solution (about 1.5 km depth) than in the CESM equilibrium (around 2 km depth).
In the barotropic streamfunction of the CESM equilibrium solution two subtropical gyre circulation cells still exist in the North and South Pacific. The magnitude of these two Pacific cells in the restoring solution is about half of those in the CESM equilibrium, which is similar to the difference in the 40 Ma 4PIC case. Cells that have a similar or slightly smaller magnitude are present in the Indian Ocean and South Atlantic as well in the CESM equilibrium, in the restoring solution these cells are present

but much weaker. In the CESM solution an ACC is present that is about two times as strong as the South Pacific subtropical gyre and about three times as strong as the ACC of the 38 Ma 4PIC CESM equilibrium solution, however, no ACC is present in our restoring solution.
The average temperature, globally, below 2000 m and for the upper 1000 m are higher than in the CESM equilibrium solution. The differences are 1 °C smaller than the differences in temperature between the 40 Ma 4PIC restoring solution and 38 Ma 4PIC CESM equilibrium solution.
The diagnosed freshwater flux of the CESM equilibrium solution has an order of magnitude and spatial pattern that is similar to that of the restoring solution, though the latter has more peaks with higher amplitudes and the former is much smoother, similar to the difference between the 40 Ma 4PIC restoring and CESM solution.

3.1.3 40 Ma bathymetry, with 2× pre-industrial greenhouse gas levels

To study the influence of CO_2 forcing separately from the influence of bathymetry, a restoring steady state is calculated for the 40 Ma paleobathymetry with forcing from a CESM equilibrium state for 38 Ma under 2× pre-industrial CO_2 forcing (38Ma 2PIC). The results are shown in Figure 3.3 and values are given in Table 3.1 and Table 3.2, indicated with 40 Ma R2. The barotropic streamfunction of this solution is very similar to the 40 Ma 4PIC restoring solution. The overturning streamfunction, temperature and salinity are very similar to the 30 Ma 2PIC restoring solution.

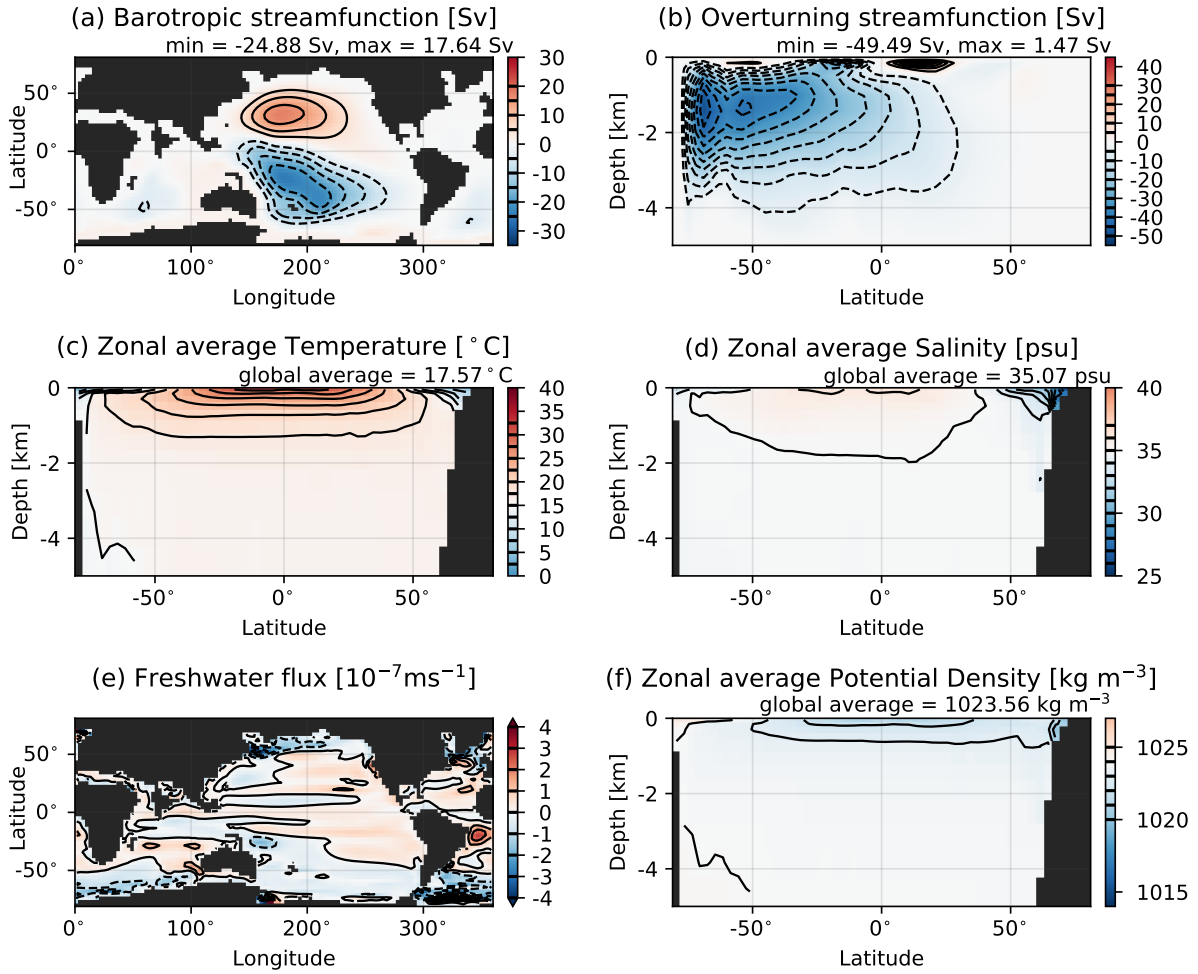

Figure 3.3: Plots of (a) barotropic streamfunction, (b) meridional overturning streamfunction, (c) zonal average temperature, (d) zonal average salinity, (e) diagnosed freshwater flux and (f) zonal average potential density for the restoring steady state solution for 40 Ma bathymetry under 38Ma 2PIC forcing. The minimum and maximum of the overturning streamfunction are calculated below a depth of 500 m.

For the 38Ma 2PIC CESM equilibrium solution itself the barotropic streamfucntion and pattern of overturning streamfunction are most similar to the 38Ma 4PIC CESM equilibrium solution, though the overturning strength is somewhat higher. The temperature and salinity are more similar to the 30Ma 2PIC CESM equilibrium solution. Hence the results of the 40 Ma 2PIC solution compared to the 40 Ma 4PIC and 30 Ma 2PIC solutions are similar for both the CESM solutions and restoring solutions.

3.2 Steady states under mixed boundary conditions

In order to investigate whether there exist other MOC states than the one found under restoring boundary conditions, we perform simulations under mixed boundary conditions, starting from the restoring steady state solutions as found in section 3.1. The diagnosed freshwater flux of these solutions is used as a boundary condition instead of restoring to a prescribed upper layer salinity field. Note that since the model directly calculates an equilibrium solution, a solution obtained under restoring boundary conditions stays, per definition, exactly the same when is switched to mixed boundary conditions. A perturbation is introduced in the freshwater flux that is compensated in the area outside the perturbation such that the total flux is zero. Using the continuation methods as described in subsection 2.1.1, a bifurcation diagram of steady state solutions dependent on the perturbation strength is computed.
Four different kind of perturbations are defined:

- **NS**: a negative perturbation in the South Pacific (60°S-30°S, 180°E-270°E) and a positive perturbation in the North Pacific (30°N-60°N, 150°E-240°E), which are locations similar to those used in Baatsen et al. (2018)
- **NSH**: also a negative perturbation in the South Pacific (81°S-60°S, 174°E-279°E) and a positive perturbation in the North Pacific (51°N-72°N, 144°E-228°E), but at higher latitudes than NS
- **S**: only a negative perturbation in the South Pacific at the same location as NSH
- **SWhole**: a negative perturbation in the entire Southern Ocean south of 60°S

The perturbation strength is defined as the magnitude of the added freshwater flux in the area of the perturbation and its sign is the same as the sign of the perturbation in the South Pacific or Southern Ocean. Converting this to a total flux in Sverdrups depends on the area of the perturbation and thus the conversion factor differs per perturbation. For example for the perturbation NSH a perturbation strength of -1×10^{-7}ms^{-1} corresponds to a decrease of 1×10^{-7}ms^{-1} in freshwater flux in the area defined in the South Pacific and an increase of 1×10^{-7}ms^{-1} in the area defined in the North Pacific. For the NSH perturbation this is the same as a total perturbation in flux of about -0.78 Sv in the South Pacific and about 0.79 Sv in the North Pacific. The extra flux of 0.01 Sv is compensated by a total flux of -0.01 Sv in the area outside both perturbations.
Instead of changing the strength of a (local) perturbation in the freshwater flux, the strength of the freshwater flux pattern as a whole can be changed as well. The original forcing strength has a value of 1 and the amplitude of the freshwater flux can be lowered or raised by respectively decreasing or increasing this value. A value of 0 corresponds to an amplitude of 0 and thus a freshwater flux that is 0 ms^{-1} everywhere.

3.2.1 40 Ma bathymetry

A bifurcation diagram is computed for each of the four perturbations for the case with 40 Ma paleobathymetry, starting from the restoring solution obtained under 38Ma 4PIC forcing (as described in subsection 3.1.1 and shown in Figure 3.1), with the diagnosed freshwater flux shown in Figure 3.1 as boundary condition. The bifurcation diagram found for all four perturbations makes a loop that ends up at the same solution as the restoring solution. Hence the branch of steady state solutions that is found only reaches a certain range in perturbation strengths. In order to finish the loop, the

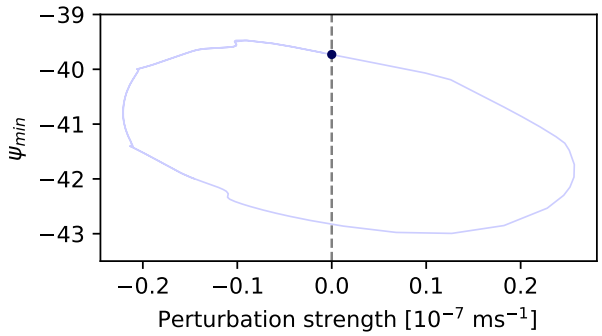

Figure 3.4: Bifurcation diagram of the minimum in overturning streamfunction, calculated over the whole water column, for perturbation NSH. A perturbation strength of -0.1×10^{-7}ms^{-1} over the area of the perturbation corresponds to a perturbation of −0.078 Sv in the South Pacific and a perturbation of 0.079 Sv in the North Pacific. The dot indicates the solution found under restoring boundary conditions as described in subsection 3.1.1 and shown in Figure 3.1.

perturbation strength switches sign (becomes positive), which means that there is a positive perturbation instead of a negative perturbation in the South Pacific or Southern Ocean and vice versa for the perturbation in the North Pacific, if it is present. An example of one of these looping bifurcation diagrams is shown in Figure 3.4. Differently form the rest of this chapter, the minimum in overturning strength in the bifurcation diagram is calculated for the whole water column, so could include surface overturning cells.

The range of perturbation strengths reached within the loop is relatively small. The lowest negative perturbation strength that is reached is with the perturbation in the South Pacific only (S) and has a value of -0.26×10^{-7}ms^{-1}, the largest positive perturbation is reached with the NSH perturbation and is 0.32×10^{-7}ms^{-1}. This minimum and maximum are almost an order of magnitude smaller than the freshwater flux itself. The range in the minimum of the overturning streamfunction, which is used as an indication of change in overturning strength with perturbation strength, is relatively small as well. The range over which the minimum in overturning strength varies is ~ 4 Sv for the NS, NSH and SWhole perturbations and ~ 8 Sv for the S perturbation, which is an order of magnitude smaller than the strength of the minimum itself, which varies around ~ 40 Sv. The MOC-state along the bifurcation diagrams obtained using the four different perturbations thus stays very close to the restoring strong southern sinking solution.

At a perturbation strength of zero, the freshwater flux is unperturbed and thus the mixed boundary conditions are the same as those of the restoring solution (same freshwater flux, upper layer temperature and wind stress forcing). Besides the restoring solution, one other solution (for perturbations NS, NSH and SWhole) or three other solutions (for perturbation S) are found to occur at a perturbation strength of zero. These additional solutions are very similar to the restoring solution, but have a slightly stronger meridional overturning. For the cases with only one additional solution, the minimum in streamfunction is about 3 Sv stronger. For the case with three additional solutions the largest difference is 3 Sv in minimum streamfunction as well, while the other two solutions have a smaller difference. The MOC pattern of these additional solutions thus stays a strong southern sinking solution.

A bifurcation diagram of the steady state solution dependent on the amplitude of the freshwater flux as a whole is computed, to see whether this has an effect on the MOC-state. The resulting bifurcation diagram again makes a loop that returns at the same solution as the restoring solution, with a range in salinity forcing of 0.99 to 1.09, where 1 corresponds to the original forcing strength. The range of the minimum in overturning streamfunction is ~ 4 Sv (varying around ~ 40 Sv). Three other solutions are found at a salinity forcing of 1, thus under the same mixed boundary conditions as the restoring solution. These three solutions have a stronger overturning than the restoring solution, with again a largest difference of 3 Sv, though still are strong southern sinking solutions.

3.2.2 30 Ma bathymetry

To see if the looping bifurcation diagram with only southern sinking MOC-states is a result of the 40 Ma paleobathymetry and forcing, a bifurcation diagram starting from the restoring steady state solution found for 30 Ma paleobathymetry under 30Ma 2PIC forcing (as described in subsection 3.1.2 and shown in Figure 3.2), with the diagnosed freshwater flux shown in Figure 3.2 as boundary condition, is computed. This is done for perturbation NSH only, as with this perturbation the highest perturbation strength was reached for the 40 Ma case. The resulting bifurcation diagram, however, again makes a loop ending up at the same solution as the restoring solution. The range in perturbation strength reached is -0.02×10^{-7}ms^{-1} to 0.63×10^{-7}ms^{-1} and the range in minimum meridional overturning streamfunction is $\sim$ 5 Sv (varying around $\sim$ 50 Sv). Hence the MOC-state again stays a strong southern sinking state along the bifurcation diagram. One other solution was found at the same mixed boundary conditions as the restoring solution that is similar to the restoring solution, but has an overturning streamfunction that is about 1 Sv weaker. As this is a similar result to the 40 Ma case, it was decided not to repeat the simulations with the other perturbations and freshwater flux amplitude for the 30 Ma case and try a different approach, as described in the following section.

3.3 Steady states under modified (salinity) forcing

As described in section 2.3 there is a north-south asymmetry in upper layer temperature and salinity forcing which may influence the preference for a certain MOC-state. In order to reduce the effect of asymmetry in upper layer temperature forcing, the temperature field is modified such that its zonal average is approximately symmetric around the equator (see subsection 2.3.1). The effect of the asymmetry in upper layer salinity is studied by performing simulations with two modified upper layer salinity forcings, which are constructed from the zonal average (ZA) of the original upper layer salinity field (see subsection 2.3.1). As a starting point, two restoring solutions are obtained the same way as described in section 3.1. The first restoring solution, that will be indicated as the original ZA restoring solution, is obtained using the unmodified wind stress forcing, symmetric temperature forcing and zonally averaged salinity forcing. The second restoring solution, indicated as mirrored ZA restoring solution is obtained using the unmodified wind stress forcing and symmetric temperature forcing as well, though with mirrored zonally averaged salinity forcing.

3.3.1 Restoring states in the 40 Ma bathymetry

Two restoring solutions, one with original ZA and one with mirrored ZA salinity forcing are obtained for the 40 Ma paleobathymetry and modified forcing based on the 38Ma 4PIC forcing. The diagnosed freshwater flux for both restoring solutions is shown in Figure 3.5, the meridional overturning streamfunction of the mirrored ZA restoring solution is shown in Figure 3.7A and the the meridional overturning streamfunction of the original ZA restoring solution is shown in Figure 3.7E. Values of each solution are given in Table 3.1 and Table 3.2, indicated by the same letters, A and E, as in Figure 3.7.

Original ZA restoring solution

The MOC-state of the original ZA restoring solution is a strong southern sinking solution, just as was found with the original forcing as described in subsection 3.1.1. The original ZA restoring solution, however, has an overturning cell that is shallower but stronger than the restoring solution with original forcing. The overturning per basin is relatively similar to the restoring solution with original forcing, though there are some small differences in strength and depth of the overturning cell. The main difference is an occurrence of a small positive cell (maximum of 6.1 Sv) near the center of the Pacific basin at about 3.5 km depth. The barotropic streamfunction is similar to that of the restoring solution with original forcing and the global average temperature and global average salinity are

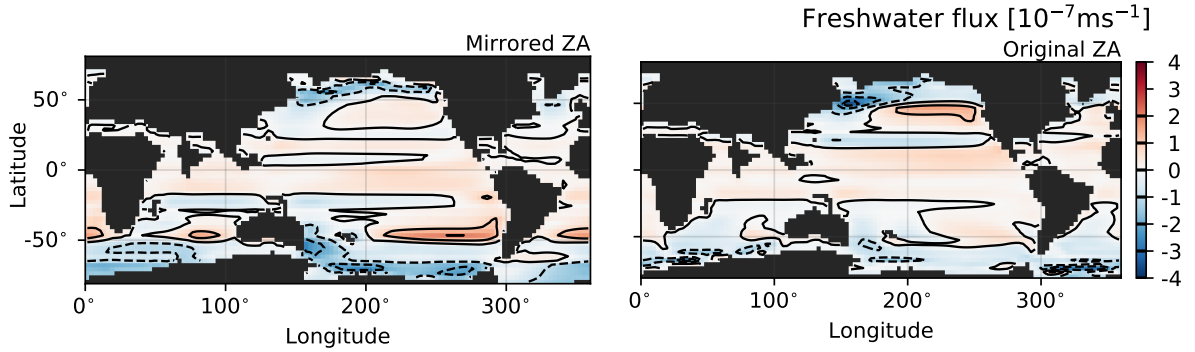

Figure 3.5: Diagnosed freshwater flux for the mirrored ZA (left) and original ZA (right) restoring solutions for 40 Ma bathymetry.

lower. Especially the Atlantic is colder (average of 18.1 °C), less saline (average of 34.7 psu) and less different from the northernmost part of the Atlantic than in restoring solution with original forcing. The zonal average potential density is very similar to the restoring solution with original forcing, with an unstable stratification in the southernmost part of the basin. Since a zonal average of the upper layer salinity is used as forcing, the diagnosed freshwater flux is more symmetric in the zonal direction as well. The order of magnitude is similar to the diagnosed freshwater flux of the restoring solution with original forcing, though the peaks have a less strong amplitude of up to about 3×10^{-7}ms^{-1}. Furthermore, most peaks are found in either the North Pacific or Southern Ocean.

Mirrored ZA restoring solution

The MOC-state of the mirrored ZA restoring solution is a strong northern sinking solution, consisting of one large positive overturning cell with a maximum below a depth of 500 m of 35.2 Sv. The strongest positive overturning cell is located in the Pacific, though in the Atlantic a weak positive overturning cell occurs as well. In the Indian and Southern Ocean barely any overturning occurs and the overturning that occurs is relatively shallow. The barotropic streamfunction of the mirrored ZA restoring solution consists, just as for the original ZA restoring solution, mainly of a positive cell in the North Pacific and negative cell in the South Pacific. Contrary to in the original ZA restoring solution, the northern cell is stronger than the southern cell. The global average temperature and salinity are (much) higher for the mirrored ZA than for the original ZA restoring solution. The difference between the northernmost Atlantic and the rest of the basin is larger for temperature and smaller for salinity in the mirrored ZA restoring solution. The unstable stratification in zonal average potential density occurs in the northernmost part of the basin, mostly in the North Pacific. The peaks in diagnosed freshwater flux occur mostly in the southern part of each basin, the Southern Ocean and the northernmost North Pacific.

The positive peaks in diagnosed freshwater flux for both the mirrored ZA and original ZA solutions seem to occur only in the hemisphere where the upper layer salinity becomes quite fresh towards higher latitudes, around the latitude where the gradient in zonal average upper layer salinity is largest. The negative peaks seem to occur mostly at high latitudes.

3.3.2 Restoring states in the 30 Ma bathymetry

Two restoring solutions, with original ZA and mirrored ZA salinity forcing are obtained for the 30 Ma paleobathymetry and a modified forcing based on the 30 Ma 2PIC forcing. The meridional overturning streamfunction of the mirrored ZA solution is shown in Figure 3.8A, that of the original ZA solution shown in Figure 3.8F and the diagnosed freshwater flux of both solutions in Figure 3.6. Values of each solution are given in Table 3.1 and Table 3.2, indicated by the same letters, A and F, as in Figure 3.8.

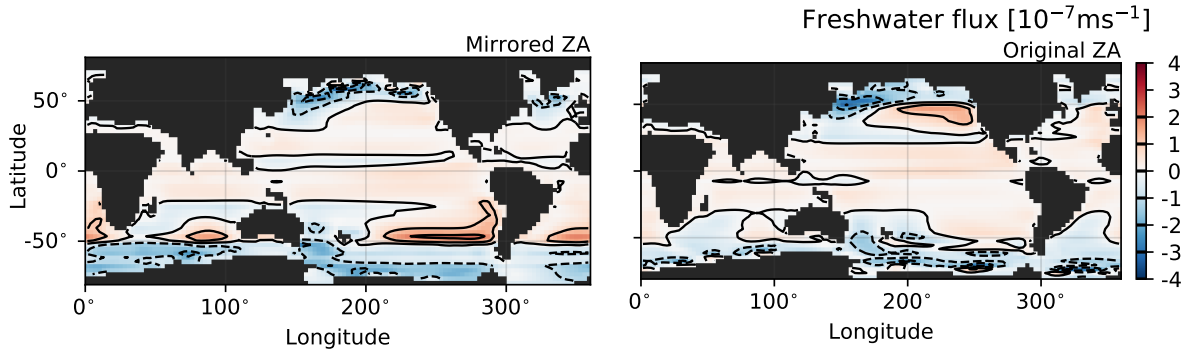

Figure 3.6: Diagnosed freshwater flux for the mirrored ZA (left) and original ZA (right) restoring solutions for 30 Ma bathymetry.

Original ZA restoring solution

The MOC-state of the original ZA restoring solution is, just as for the 40 Ma case, a strong southern sinking solution that is slightly weaker than that of the restoring solution with the original forcing as described in subsection 3.1.2 and slightly stronger with a cell that reaches a greater depth than that of the 40 Ma original ZA restoring solution. The overturning is again negative in each basin, though there are some differences in strength compared to the restoring solution with original forcing and 40 Ma original ZA restoring solution. The barotropic streamfunction is slightly stronger than that of the restoring solution with original forcing. Both the global average temperature and salinity are lower than in the restoring solution with original forcing, which is also the case for the average temperature and salinity of each basin separately. The zonal average potential density is again relatively similar to that of the restoring solution with original forcing, with unstable stratification in the southernmost part of the basin. Furthermore the diagnosed freshwater flux is more symmetric in zonal direction and has peaks with a weaker amplitude of up to about 3×10^{-7}ms^{-1} when compared to that of the restoring solution with original forcing. The spatial pattern in diagnosed freshwater flux is relatively similar to that of the 40 Ma original ZA restoring solution.

Mirrored ZA restoring solution

The mirrored ZA restoring solution has, just as for the 40 Ma case, a strong northern sinking MOC-state that is slightly stronger than that of the 40 Ma mirrored ZA restoring solution. Similar to the 40 Ma solution, the strongest positive overturning cell is located in the Pacific, a weaker positive overturning cell in the Atlantic and barely any overturning occurs in the Indian Ocean and Southern Ocean. The barotropic streamfunction is similar as well, with slightly stronger cells. The global average temperature and salinity are higher than for the original ZA restoring solution, just as for the 40 Ma case. Just as for the 40 Ma case as well, the difference between the northernmost Atlantic and the rest of the basin compared to the original ZA restoring solution is larger for temperature and smaller for salinity. The zonal average potential density has an unstable stratification in the northernmost part of the basin, mostly in the North Pacific. The diagnosed freshwater flux is similar to that of the 40 Ma mirrored ZA restoring solution, with peaks of up to about 3×10^{-7}ms^{-1}.

3.3.3 Bifurcation diagram for the 40 Ma bathymetry

To study the possibility of a connection of the southern sinking state of the original ZA solution to the northern sinking state of the mirrored ZA restoring solution, a bifurcation diagram is calculated under mixed boundary conditions for a change in freshwater flux forcing. This is done using a salinity homotopy parameter that describes a linear combination of the diagnosed freshwater flux fields of the mirrored ZA and original ZA restoring solutions. The freshwater flux field F_H that is used as boundary condition, dependent on the value of the salinity homotopy α_H, is defined as in Equa-

tion 2.3 in subsection 2.1.1. The freshwater flux at salinity homotopy = 0 (F_0 in Equation 2.3) is defined to be the diagnosed freshwater flux of the mirrored ZA restoring solution, the freshwater flux at salinity homotopy = 1 (F_1 in Equation 2.3) the diagnosed freshwater flux of the original ZA restoring solution. To clarify, a salinity homotopy of 0.25, for example, corresponds to a freshwater flux as boundary condition that is 0.25 times the diagnosed freshwater flux of the mirrored ZA restoring solution plus 0.75 times the diagnosed freshwater flux of the original ZA restoring solution. This is the same for negative perturbations or perturbations above a value of 1. For example, a salinity homotopy of −0.5 corresponds to a freshwater flux as boundary condition that is −0.5 times the diagnosed freshwater flux of the mirrored ZA restoring solution plus 1.5 times the diagnosed freshwater flux of the original ZA restoring solution. As all steady state solutions found with the same value for salinity homotopy have the same freshwater flux field as boundary condition and other boundary conditions are not changed, these solutions all have the same mixed boundary conditions.

A continuation is performed both starting from the mirrored ZA (red line) and original ZA (blue line) restoring solutions for 40 Ma paleobathymetry that are described in subsection 3.3.1. The resulting bifurcation diagram is shown in Figure 3.7. A salinity homotopy of zero corresponds to a freshwater flux forcing as shown in Figure 3.5, left and a salinity homotopy of one to a freshwater flux forcing as shown in Figure 3.5, right. From the two starting restoring solutions a continuation is performed both starting in positive and in negative direction of salinity homotopy. For the branch starting with the original ZA solution (blue line) the continuation is stopped when a salinity homotopy of −1 is reached and in the other direction when a salinity homotopy of 0 is reached, which is the solution marked with B in Figure 3.7. The branch starting with the mirrored ZA solution (red line) is continued to a salinity homotopy of 1.5 in one direction and until a salinity homotopy of 0.4 (in between the solutions marked B and E in Figure 3.7) is reached in the other direction, as the branch was found to overlap with the original ZA branch.
The metric of the steady state solutions used in the bifurcation diagram is the sum of the minimum and maximum in meridional overturning streamfunction below 500 m depth, $\psi_{min} + \psi_{max}$, which provides a measure of the asymmetry in MOC-state. When $\psi_{min} + \psi_{max}$ is positive (negative), the

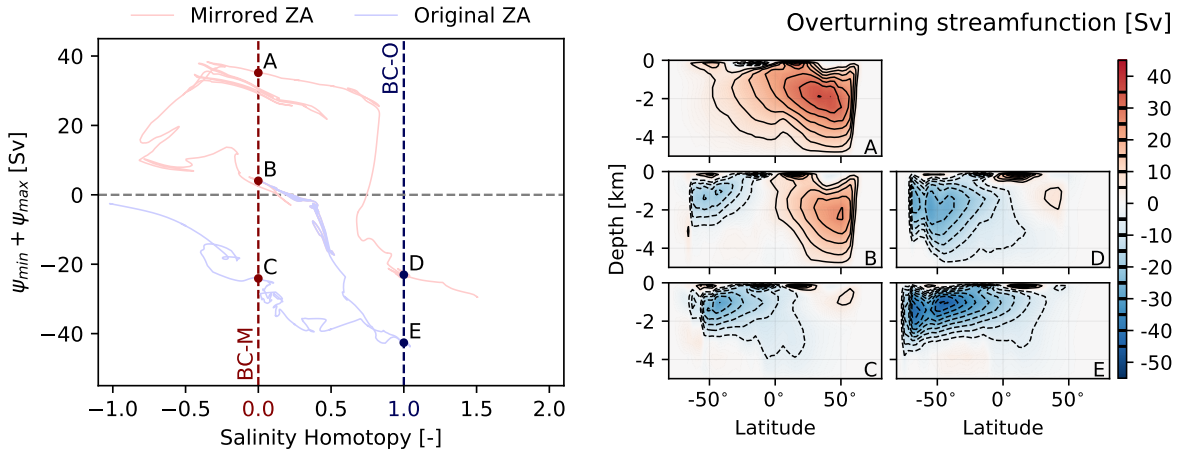

Figure 3.7: Bifurcation diagram (left) of the sum of the minimum and maximum in meridional overturning streamfunction below 500 m depth, $\psi_{min} + \psi_{max}$, as a function of salinity homotopy for a 40 Ma paleobathymetry and (right) plots of the global meridional overturning streamfunction corresponding to the steady state solutions marked in the bifurcation diagram at salinity homotopy of zero and one. The solution at A is the mirrored ZA restoring solution, the solution at E the original ZA restoring solution. Salinity homotopy = 0 (marked by the red dashed line and BC-M) corresponds to forcing with the freshwater flux as shown in Figure 3.5, left and salinity homotopy = 1 (marked by the blue dashed line and BC-O) to that as shown in Figure 3.5, right. The red line in the bifurcation diagram indicates the steady state solutions computed starting from the mirrored ZA restoring solution, the blue line to steady state solutions computed starting from the original ZA restoring solution.

positive overturning cell is stronger (weaker) than the negative overturning cell, indicating a northern (southern) sinking state, with a greater magnitude of $\psi_{min}+\psi_{max}$ indicating that this MOC-state is stronger. When $\psi_{min}+\psi_{max}$ is relatively close to zero, the positive and negative cell are similar in strength, indicating a bipolar sinking state. Some of the steady state solutions found under a salinity homotopy of zero and one, including the two restoring solutions the continuation is started from, are marked in the bifurcation diagram and their global meridional overturning streamfunctions are shown in Figure 3.7. Values of these five marked solutions are given in Table 3.1 and Table 3.2, indicated by the same letters as in Figure 3.7. The overturning streamfunction per basin of each marked solution, including the minimum and maximum overturning strength per basin, are shown in Appendix A, again indicated by the same letters.

Original ZA mixed boundary conditions

The solution with the strongest southern sinking MOC-state is the original ZA restoring solution (E in Figure 3.7). As described in subsection 3.3.1, this solution has a negative overturning in each basin and a minimum in global meridional overturning streamfunction below 500 m of -45.8 Sv. With the same mixed boundary conditions, another, weaker southern sinking state is found (D) that has a global overturning with a minimum of -29.9 Sv. The overturning per basin, however, is quite different; the negative overturning cell in the Pacific is much weaker than for the original ZA restoring solution, in the Indian Ocean barely any overturning occurs and in the Atlantic there is a weak positive overturning cell with a maximum of 9.2 Sv. The negative overturning in the Southern Ocean, though, is still quite strong. This overturning pattern is closer to the present-day MOC than the original ZA solution, though compared to present-day it has a weaker positive overturning in the Atlantic and a stronger negative overturning in the Pacific. The barotropic streamfunction of solution D has a stronger cell in the South Pacific and a slightly weaker cell in the North Pacific. Global average temperature and salinity of solution D are both higher than those of the original ZA restoring solution, this is true for each basin separately as well.

Mirrored ZA mixed boundary conditions

The solution with the strongest northern sinking MOC-state is the mirrored ZA restoring solution (A in Figure 3.7) that, as described in subsection 3.3.1, has a positive overturning in all basins and a maximum in global meridional overturning streamfunction below 500 m of 35.2 Sv. With the same mixed boundary conditions a weaker northern sinking state, a bipolar sinking state (B) and a weak southern sinking state (C) are found as well. The bipolar solution (B) has a strong positive overturning cell in the Pacific and negative overturning cells in the other basins. The southern sinking solution (C) has only some very small positive overturning cells in the Pacific and negative overturning cells in the other basins. The barotropic streamfunction of solution B is very similar to that of the mirrored ZA restoring solution. For solution C both cells are weaker, though a small negative cell occurs in the Indian Ocean. Both solutions B and C have a lower global temperature and salinity compared to the mirrored ZA restoring solution, for each basin separately as well. Compared to solution B, solution C has a higher average temperature in the Atlantic and Indian Ocean, a lower average temperature in the Pacific and a slightly lower temperature in the Southern Ocean. The average salinity is higher in the Atlantic and Indian Ocean and lower in the Pacific as well, but higher in the Southern Ocean.

For all five solutions (A-E), the zonal average potential density is in general unstably stratified near the locations where deep water formation occurs.

3.3.4 Bifurcation diagram for the 30 Ma bathymetry

A bifurcation diagram under mixed boundary conditions for a change in salinity homotopy and starting from the mirrored ZA and original ZA restoring solutions (see section subsection 3.3.2) is calculated the same way as described in subsection 3.3.3. The freshwater flux at salinity homotopy $= 0$

is the diagnosed freshwater flux of the mirrored ZA restoring solution as shown in Figure 3.6, left, the freshwater flux at salinity homotopy = 1 that of the original ZA restoring solution as shown in Figure 3.6, right. The resulting bifurcation diagram and the meridional overturning streamfunctions of six marked steady state solutions found at a salinity homotopy of zero and one are shown in Figure 3.8. The branch (red line) starting from the mirrored ZA restoring solution (A in Figure 3.8) is continued in one direction until a salinity homotopy of −1 is reached and in the other direction until a salinity homotopy of 1.5 is reached. The branch (blue line) starting from the original ZA restoring solution (F in Figure 3.8) makes a loop that ends up at the original ZA restoring solution again. Values of these six marked solutions are given in Table 3.1 and Table 3.2, indicated by the same letters as in Figure 3.8. The overturning streamfunction per basin of each marked solution, including the minimum and maximum overturning strength per basin, are shown in Appendix A, again indicated by the same letters.

Original ZA mixed boundary conditions

Multiple solutions with southern sinking MOC-states are found with the same mixed boundary conditions (salinity homotopy = 1) as the original ZA restoring solution (F) that is described in subsection 3.3.2. Of these solutions, the original ZA restoring solution has the strongest meridional overturning streamfunction, with a minimum below 500 m of −47.4 Sv. The weakest southern sinking solution (D), has a minimum of −33.4 Sv and the marked southern sinking solution in between (E) a minimum of −36.9 Sv. These solutions D and E have a negative overturning that is strongest in the Southern Ocean, then in the Pacific and then in the Indian Ocean, which is similar to in the original ZA restoring solution. The overturning in the Atlantic, however, is positive for solutions D and E, though this positive overturning is relatively weak. The barotropic streamfunction of solutions D and E is very similar as well. The global average temperature and salinity of both solutions D and E are higher than for the original ZA restoring solution. This is the case for each basin separately as well, though the especially the difference between the average temperature in the Pacific of solutions D, E and F is relatively small.

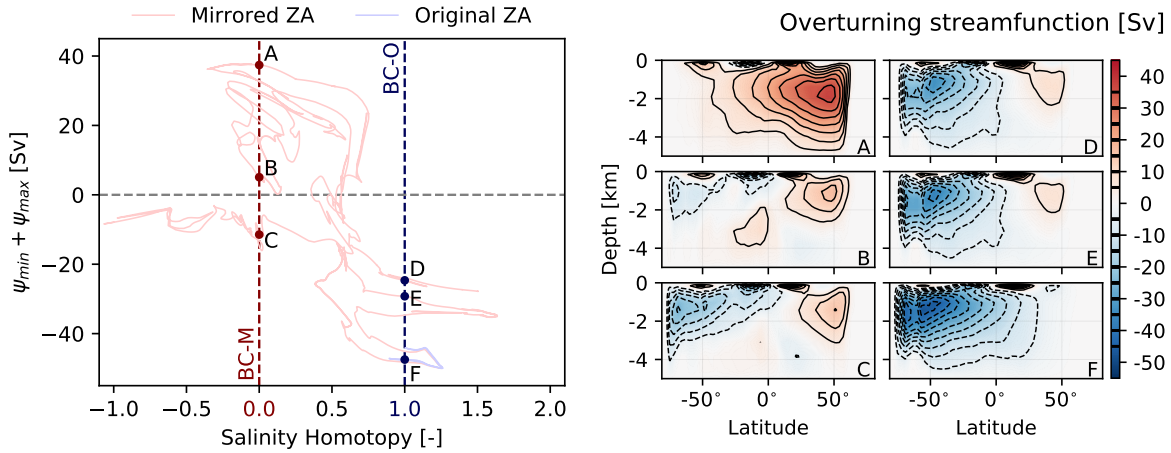

Figure 3.8: Bifurcation diagram (left) of the sum of the minimum and maximum in meridional overturning streamfunction below 500 m depth, $\psi_{min} + \psi_{max}$, as a function of salinity homotopy for a 30 Ma paleobathymetry and (right) plots of the global meridional overturning streamfunction corresponding to the steady state solutions marked in the bifurcation diagram at salinity homotopy 0 and 1. The solution at A is the mirrored ZA restoring solution, the solution at F the original ZA restoring solution. Salinity homotopy = 0 (marked by the red dashed line and BC-M) corresponds to forcing with the freshwater flux as shown in Figure 3.6, left and salinity homotopy = 1 (marked by the blue dashed line and BC-O) to that as shown in Figure 3.6, right. The red line in the bifurcation diagram indicates the steady state solutions computed starting from the mirrored ZA restoring solution, the blue line to steady state solutions computed starting from the original ZA restoring solution.

Mirrored ZA mixed boundary conditions

With the same mixed boundary conditions as the mirrored ZA restoring solution (A), that is described in subsection 3.3.2, several steady state solutions occur. Of these solutions, the mirrored ZA restoring solution has the strongest northern sinking MOC-state, with a maximum below 500 m of 37.5 Sv and positive overturning in each basin. The MOC-state of the other solutions ranges from a weaker northern sinking solution, to a bipolar solution with stronger northern sinking (B) and a bipolar solution with stronger southern sinking (C). The first bipolar solution (B) has small positive overturning cells in the Pacific and Atlantic and small negative overturning cells in the Indian Ocean and Southern Ocean. The second bipolar solution (C) has positive overturning cells in the Pacific at the same locations as solution B, but slightly stronger and negative overturning cells in the Southern Ocean, Indian Ocean and Atlantic. The two bipolar solutions (B and C) have a barotropic streamfunction that is similar to that of the mirrored ZA restoring solution. The global average temperature of solutions B and C is lower than mirrored ZA restoring solution, though the global average salinity is the same. For solution B the average temperature of all basins separately is colder than in the mirrored ZA restoring solution, for solution C the average temperature per basin is even colder. For solution B the Pacific is less saline, the Atlantic more saline and the salinity of the Indian Ocean and Southern Ocean similar to in the mirrored ZA restoring solution. The salinity per basin of solution C is relatively similar to that in the mirrored ZA restoring solution, though generally in solution C the salinity near the surface is somewhat lower in the northern part of the basins and somewhat higher in the southern part.

The zonal average potential density for all six solutions (A-F) is in general unstably stratified near the locations where deep water formation occurs.

3.3.5 Meridional heat transport for the 40 Ma and 30 Ma bathymetries

In order to study the distribution of heat in the different steady state solutions found for 40 Ma and 30 Ma, the meridional heat transport is calculated (see definition in subsection 2.1.3). The results are shown in Figure 3.9, with the letters indicating the same solutions as in Figure 3.7 and Figure 3.8. The global average meridional heat transport is shown in the figure for each solution, with the color indicating the main direction of transport.
The global average heat transport is northward in the predominantly northern sinking solutions and southward in the predominantly southern sinking solutions. Heat is transported towards high latitudes in the hemisphere where sinking occurs, though in the other hemisphere the meridional heat transport is small or even almost absent, such as for the strong southern sinking only solutions (E for 40 Ma and F for 30 Ma). Furthermore, in most of these solutions heat is transported towards the hemisphere with sinking from the opposite hemisphere. In the bipolar sinking solutions the meridional heat transport is more even for both hemispheres, though there still is a small preference for southward transport. In the 40 Ma bipolar sinking solution a small amount of heat is distributed across the equator towards the northern hemisphere, while in the 30 Ma bipolar sinking solution a small amount of heat is distributed across the equator towards the southern hemisphere.
Compared to the CESM solutions from Baatsen (2019) there is much more asymmetry between both hemispheres in the meridional heat transport of the southern sinking solutions. Especially the transport in the northern hemisphere is much weaker, as in the CESM solution it is similar in order of magnitude to the transport in the southern hemisphere. This results in a much stronger southward heat transport than is observed for the CESM solutions. Furthermore, in the CESM solutions the heat transport for the 30 Ma case is slightly stronger in the northern hemisphere than for the 40 Ma case, which is something not observed here.

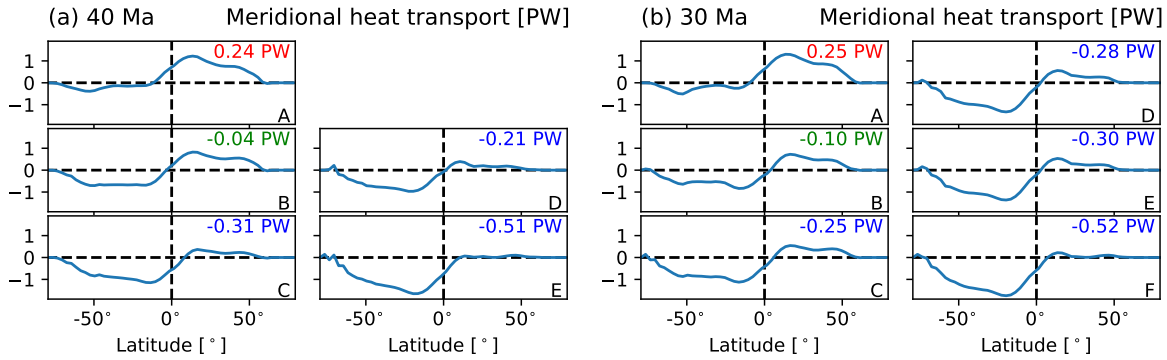

Figure 3.9: Meridional heat transport for 40 Ma (a, letters correspond to solutions in Figure 3.7) and 30 Ma (b, letters correspond to solutions in Figure 3.8). The global average meridional heat transport of each solution is displayed in the upper right corner. A net northward transport is given in red, a net southward transport in blue and a transport that is approximately symmetric in green

4 Discussion

4.1 Steady states under restoring boundary conditions

In the first part of the results (see section 3.1), equilibrium ocean states are obtained with restoring boundary conditions for a 40 Ma paleobathymetry with 38 Ma 4PIC forcing and a 30 Ma paleobathymetry with 30 Ma 2PIC forcing. Note that the simulations with 30 Ma paleobathymetry are more representative of a Late Eocene climate due to the absence of ice and hence no Antarctic ice sheet in the model and the absence of an Antarctic ice sheet in the CESM simulations where the forcing is taken from (Baatsen, 2019). For both cases a strong southern sinking pattern in Meridional Overturning Circulation (MOC) is found, which is slightly stronger for the 30 Ma case. The barotropic streamfunction for both cases consists of two circulation cells, a positive (clockwise) cell in the North Pacific and a stronger negative (anticlockwise) cell in the South Pacific, that have a larger difference in strength for the 30 Ma case and roughly correspond to subtropical gyres. In the Late Eocene the Pacific is by far the largest basin, larger than in the present-day, while the Atlantic basin is smaller than in the present-day. Hence, most of the circulation, both wind-driven and overturning circulation, is expected to occur in the Pacific basin opposed to in the Atlantic basin. The main difference between the 40 Ma and 30 Ma cases is that the temperatures are a few degrees higher (and consequentially the potential density lower) for the 40 Ma case, which is a direct effect of the higher temperature forcing for this case. Apart from this, the solutions for both cases are relatively similar.

An extra restoring solution for a 40 Ma paleobathymetry with 38 Ma 2PIC forcing is calculated to see which differences between the 40 Ma 4PIC and 30 Ma 2PIC solutions are due to the influence of bathymetry and which are due to the influence of CO_2 forcing. The barotropic streamfunction seems to be mostly affected by bathymetry, as the barotropic streamfunction of the 40 Ma 2PIC solution is very similar to the one of the 40 Ma 4PIC solution. The higher temperatures for the 40 Ma 4PIC case are mostly due to the difference in CO_2 forcing, since the temperatures in the 40 Ma 2PIC forcing and solution are similar to those in the 30 Ma 2PIC forcing and solution. The overturning streamfunction of the 40 Ma 2PIC solution is most similar in strength to that of the 30 Ma 2PIC solution, suggesting that the overturning strength might be more influenced by CO_2 forcing than bathymetry in this case.

4.1.1 Restoring steady states compared to literature

The two subtropical gyres in the North and South Pacific of the barotropic streamfunction are found in the results from Baatsen (2019) and Mulder et al. (2017) as well, though there the barotropic streamfunction is about twice as strong, more detailed and contains circulation cells in other basins. The small overturning cells near the surface are stronger as well and reach a greater depth. The differences in barotropic streamfunction and surface cells in overturning streamfunction seem to be mostly a result of the difference in value of the horizontal mixing coefficient of momentum, A_H. This because simulations with a more realistic lower value of A_H and the results in Mulder et al. (2017) and Baatsen (2019) all show a similar more detailed pattern and stronger circulation and overturning surface cells compared to the simulations with a higher value of A_H done here. The main difference between the simulations in Baatsen (2019) and in both Mulder et al. (2017) and this project is the respective presence and absence of an Antarctic Circumpolar Current (ACC). This is possibly a result of the coarser horizontal resolution of 3° used in this project and in Mulder et al. (2017) compared to the finer resolution of 1° in Baatsen (2019), in combination with the difference in A_H. The coarser horizontal resolution might result in the gateways not being wide and deep enough in order to allow for an ACC to occur. Further research, for example by repeating the simulations with a finer horizontal resolution, is needed in order to study the presence or absence of an ACC accurately.

The MOC-pattern that is found under restoring boundary conditions, a strong southern sinking pattern (negative/southward overturning), agrees with the CESM simulations from Baatsen (2019), the indications from Eocene proxies (see introduction, Hutchinson et al. (2020)) and the results from Mulder et al. (2017). Compared to the results from Baatsen (2019), however, the overturning is twice as strong and there are some differences in overturning pattern of which the most notable are shallower surface overturning cells, an overturning minimum that is located at shallower depth and the absence of a small positive (northward) overturning cell in the 30 Ma solution. The same differences are observed when comparing to the results from Mulder et al. (2017), except for the overturning strength, which is much more similar. The differences in overturning strength might be a result of a combination of two different factors: the vertical resolution in Baatsen (2019) is much larger with an amount of 60 vertical layers compared to 12 vertical layers in this project and in Mulder et al. (2017) and in Baatsen (2019) a different, variable version of vertical mixing is used. The differences in the strength and depth of surface overturning cells, and possibly the depth of the overturning minimum, are probably linked to the differences in barotropic streamfunction, which is also weaker in this project due to a higher horizontal mixing of momentum (see previous paragraph). Especially the presence of an ACC in Baatsen (2019), which is much stronger than the other circulations cells in the 30 Ma solution, might be related to the difference in MOC-pattern as the surface overturning cell in the Southern Ocean reaches to a much greater depth. The difference in vertical resolution might cause differences in the overturning pattern as well, as this allows for especially the surface layers to be much better resolved.
As the MOC is stronger and the wind-driven circulation weaker compared to the CESM simulations from Baatsen (2019), the meridional heat transport is more strongly influenced by the MOC. This results in more asymmetry between both hemispheres opposed to the meridional heat transport observed in the CESM simulations, which are more strongly influenced by the wind-driven circulation and hence more symmetric between both hemispheres. This does, however allow for the effect of the MOC on the meridional heat transport to be more clearly visible.
The temperatures observed are much higher compared to the results from Baatsen (2019) and Mulder et al. (2017). This is probably a result of the absence of a convective adjustment scheme, as in simulations without convective adjustment compared to the simulations with convective adjustment higher ocean temperatures are found as well. In the simulations without convective adjustment, an unstable stratification is mostly found to occur at the locations where deep water formation occurs, which is at one or both poles. Extra mixing at these locations would cause colder and fresher water to be mixed, resulting in a lower and fresher global temperature and salinity.

The differences between the results from this project and the results from other studies, specifically those from Baatsen (2019) and Mulder et al. (2017) are, as discussed above and in subsection 2.1.2, for a large part linked to differences in parametrisations, parameter choices and model resolution. Apart from these differences, which are mostly differences in the relative magnitude of variables and details of the patterns, many main features and characteristics of the solutions are similar. Therefore, we consider our simulated southern sinking MOC-pattern as representative of the Late Eocene, as simulations (Baatsen, 2019; Mulder et al., 2017) and proxies (Hutchinson et al., 2020) suggest.

4.1.2 Restoring steady states under modified (salinity) forcing

At the beginning of the third part of the results (see section 3.3), equilibrium ocean states are obtained with restoring boundary conditions and the same two paleobathymetries and forcings as in the first part of the results, 40 Ma 4PIC and 30 Ma 2PIC, though the upper layer forcing fields are modified (see subsection 2.3.1). The simulations with the original, though zonally averaged salinity forcing (water freshest in northern high latitudes) are referred to as original ZA, the simulations with the mirrored zonally averaged salinity forcing (water freshest in southern high latitudes) as mirrored ZA (see section 3.3).
The restoring solutions found for 40 Ma and 30 Ma with original ZA modified boundary conditions

are very similar to the restoring solutions with unmodified boundary conditions as discussed above, with strong southern sinking solutions. The overturning pattern in the solution for 40 Ma, though, differs somewhat in that the main overturning cell is shallower and a very weak positive overturning is found in the deeper part of the Pacific. Why this difference occurs is unclear, possibly there is a preference of a slightly different strong southern sinking MOC-pattern under the original ZA boundary conditions. For the mirrored ZA modified boundary conditions a strong northern sinking overturning pattern is found that is very similar for both the 40 Ma and 30 Ma cases. In these solutions positive (northward) overturning mainly occurs in the northern part of the Pacific and to a lesser degree in the Atlantic. Thus mirroring the upper layer salinity field around the equator results in a shift from a strong southern sinking solution to a strong northern sinking solution.

When considering all the simulations with restoring boundary conditions discussed in the results and in this section, the north-south asymmetry in upper layer salinity forcing seems to determine the location of sinking; a strong southern sinking MOC-state is found if the water at high latitudes is freshest in the northern hemisphere (non-modified forcing and original ZA modified forcing) and a strong northern sinking MOC-state if the water at high latitudes is freshest in the southern hemisphere (mirrored ZA modified forcing). The idea that the direction of overturning in the Pacific depends on the difference in salinity at higher latitudes agrees with the results of Baatsen et al. (2018), where both a northern sinking and a southern sinking solution were found in the same paleobathymetry, using a salinity perturbation. A freshening of the South Pacific and salinification of the North Pacific was found to coincide with the switch from a southern sinking to a northern sinking state. This is in line with the results found in this project. Of the two main circulation cells in barotropic streamfunction that are found, the cell in the hemisphere where sinking occurs seems to be strongest.

4.2 Steady states under mixed boundary conditions

4.2.1 Bifurcation diagrams of perturbation and freshwater flux strength

Since the model directly calculates equilibrium solutions, the restoring solutions as discussed in the previous section remain, per definition, the same when is switched to mixed boundary conditions. The mixed boundary conditions do, however, allow for more possible continuation parameters and allow the solution to be less restricted when a continuation is performed. In the second part of the results (see section 3.2), bifurcation diagrams of equilibrium solutions under mixed boundary conditions, dependent on the perturbation strength of four different perturbations or strength of the freshwater flux as a whole are calculated, starting from the 40 Ma 4PIC restoring solution from section 3.1. Starting from the 30 Ma 2PIC restoring solution a bifurcation diagram of only one of the perturbations is calculated. In all six cases the bifurcation diagram is found to be a small loop around the restoring solution in which the overturning strength only changes by a few Sverdrup. This gives a strong indication that the southern sinking solutions for 40 Ma and 30 Ma are isolated. It also means that under this forcing the southern sinking solution is quite dominant. The isolation might be an artificial result that is due to asymmetry in the forcing fields and/or bathymetry or due to a numerical effect. It might also be the case that no other solutions exist for this combination of parameters or that there is no connection between the strong southern sinking solution and other possible solutions. To further study this, it would be interesting to repeat the simulations with the forcing fields and/or bathymetry smoothed out or made more symmetric and see if the solution is still isolated.

4.2.2 Bifurcation diagrams with modified (salinity) forcing

In the third part of the results (see section 3.3), a bifurcation diagram is calculated for a linear deformation between two freshwater flux fields, which is described by a salinity homotopy parameter and can also be interpreted as a relatively complex freshwater flux perturbation. The first field

is the diagnosed freshwater flux of the restoring northern sinking solution obtained with mirrored ZA modified boundary conditions, the second field is the diagnosed freshwater flux of the restoring southern sinking solution obtained with original ZA modified boundary conditions. One of the starting points is the restoring northern sinking solution with mirrored ZA boundary conditions, the other the restoring southern sinking solution with original ZA boundary conditions. For the 40 Ma case the branches starting from both solutions are found to overlap and thus the bifurcation diagram consists of one long branch. For the 30 Ma case the branch starting from the northern sinking solution is similar to the branch of the 40 Ma case, while the branch starting from the southern sinking solution is an isolated loop. This isolation might be an (artificial) result due to the same reasons as mentioned in subsection 4.2.1. Notable is that the branch connected to the other solutions passes this isolated branch very closely and includes a strong southern sinking solution that is very similar to the restoring southern sinking solution. It would be interesting to further study what the differences are between these two solutions and why they are not connected to each other.
The 'messiness' of the branches, bending and going back and forth at some points, resulting in multiple relatively similar solutions in the bifurcation diagram, might also be an numerical effect or occur artificially due to asymmetry. Without these effects the bifurcation diagram is expected to be more smooth with less very similar equilibrium solutions, though this is something that requires more research. Even though not every solution in the bifurcation diagram might be physical, several qualitatively different MOC-states can be distinguished, which include northern sinking, bipolar sinking and southern sinking states. These different states are found for both the 40 Ma and 30 Ma cases, hence the possibility of different MOC-states to occur seems independent of which paleobathymetry is used. This agrees with and expands on the results from Baatsen et al. (2018), where a northern sinking and southern sinking MOC-states were found to be possible in one paleobathymetry. Furthermore, in the main part of the bifurcation diagram multiple qualitatively different equilibrium MOC-states are found to occur under the same mixed boundary conditions. The occurrence of multiple equilibria thus seems to be relatively independent on the exact freshwater flux forcing, though it does determine which equilibria occur.

A change from one of the different MOC-states to another can occur in two different ways. The first is by changing the freshwater flux field with the salinity homotopy parameter which changes the equilibrium MOC-state along the branch. This is the way the bifurcation diagram is obtained, requires a relatively large change in freshwater flux and changes the equilibrium in a continuous way. As the bifurcation diagram for 40 Ma and the main part of the diagram for 30 Ma consist of one large branch, most solutions are connected in this way. The second way is possible when multiple equilibrium MOC-states occur for the same boundary conditions, then a jump from one equilibrium to another might occur, for example due to a small random perturbation in freshwater flux. This is what is meant with the shift from one ocean circulation state to another that is proposed as one of the mechanisms behind the rapid cooling around the Eocene-Oligocene Transition (EOT) (Tigchelaar et al., 2011). To understand which equilibria and changes are likely to occur, stability analysis of the solutions is needed to see which parts of the branches are stable an when they become unstable, which is a subject for future research. Stability analysis might also uncover bifurcation points and directions to search for possibly undiscovered branches and connections in the bifurcation diagram. For now we can observe that multiple equilibrium solutions do exist under a range of possible boundary conditions, which suggests that a shift between these equilibrium MOC-states around the time of the EOT could be possible. A few qualitatively different solutions under the same mixed boundary conditions as the original ZA and mirrored ZA restoring solutions are picked to study the multiple equilibrium MOC-states that occur more closely.

Equilibrium states under original ZA mixed boundary conditions

Under the mixed boundary conditions derived from the original ZA restoring solution, only MOC-states with mostly or only southern sinking are found. Hence there seems to be a preference for a

southern sinking state in the original ZA case, though with a shift possible from a fully southern sinking state to a southern sinking state with positive overturning in the Atlantic. The latter overturning pattern is quite similar to the pattern found in Mulder et al. (2017). Even though the northern sinking in the Atlantic found in these solutions is quite weak, this shift is in line with the proposed onset or strengthening of the Atlantic Meridional Overturning Circulation (AMOC) around the time of the EOT (Hutchinson et al., 2020) and with the MOC-shift proposed in Tigchelaar et al. (2011).
The meridional heat transport of the solutions with weak northern sinking in the Atlantic is weaker southward in the southern hemisphere and slightly stronger northward in the northern hemisphere compared to the strong southern sinking solution. This results in a global average meridional heat transport that is still southward but much weaker compared to in the strong southern sinking solution. This suggest cooler southern hemisphere high latitudes and warmer northern hemisphere high latitudes for a MOC-pattern with weak Atlantic overturning compared to a MOC-pattern with only southern sinking. The global average (and deep ocean) temperatures show an increase when shifting to a state with weak northern sinking in the Atlantic. This is opposite to the decrease in temperatures across the EOT as is observed in proxies (Hutchinson et al., 2020), but similar to what is observed in Baatsen et al. (2018) when changing from a southern sinking to a northern sinking state. However, similar to the argumentation in Baatsen et al. (2018), the restoring boundary conditions for upper layer temperature allow little adaptation of sea surface temperatures and thus the source of deep water to a change in MOC-pattern. Hence the temperature changes in the model are strongly dependent on the prescribed upper layer temperature field and possibly do not give a good representation of the effects of a MOC-change. More research, for example with the model extended to include an (simple) atmosphere, is needed for a better understanding of the effects of a MOC-change on sea surface and deep ocean temperatures.

Equilibrium states under mirrored ZA mixed boundary conditions

Under the mixed boundary conditions derived from the mirrored ZA restoring solution a range of different MOC-states is possible, ranging from a fully northern sinking to a bipolar and weak southern sinking solution. All of these solutions, though, show a positive overturning in the Pacific, while in the other basins both positive and negative overturning is found to occur. Hence the direction of overturning in the Pacific seems to be more dependent on the mixed boundary conditions (freshwater flux) than is the case for the other basins, as it is positive with mirrored ZA mixed boundary conditions and negative with original ZA mixed boundary conditions. The direction of overturning in the Atlantic seems to be less dependent on the mixed boundary conditions as both positive and negative overturning occur with both mirrored ZA and original ZA mixed boundary conditions. With mirrored ZA mixed boundary conditions, and thus a positive overturning in the Pacific, more MOC-states seem to be possible than with original ZA mixed boundary conditions and thus negative overturning in the Pacific. Furthermore, the main positive circulation cell in the northern hemisphere of the barotropic streamfunction seems to be strongest with mirrored ZA mixed boundary conditions and the main negative circulation cell in the southern hemisphere seems to be strongest with original ZA mixed boundary conditions.

Differences between 40 Ma and 30 Ma

For the 30 Ma paleobathymetry more different MOC-states are found than for the 40 Ma paleobathymetry, though the main characteristics of the solutions found are similar for both the 40 Ma and 30 Ma paleobathymetries. It is not possible to say whether the differences that are observed between the 40 Ma and 30 Ma cases is due to the difference in paleobathymetry or due to the difference in upper layer forcing. A good way to interpret these two cases is as a range of possible forcings/bathymetries around the EOT where the 40 Ma and 30 Ma paleobathymetries provide an uncertainty in bathymetry and the 38 Ma 4PIC and 30 Ma 2PIC forcings provide an uncertainty in climate around the EOT. In both cases it is possible to find different MOC-patterns, and the charac-

teristics of these patterns are relatively similar. This confirms the possibility of a shift in MOC-pattern around the EOT, independent of the exact timing of e.g. gateway openings and of the exact climate, e.g. of CO_2 levels. Furthermore, as for the combination of 30 Ma paleobathymetry and 30 Ma 2PIC forcing more different MOC-states are found, especially more states under original ZA boundary conditions with weak northern sinking in the Atlantic, it might be more susceptible for a MOC-shift than the combination of 40 Ma paleobathymetry and 38 Ma 4PIC forcing.

5 Conclusions

In this project the global ocean circulation, specifically the possibility of different patterns in Meridional Overturning Circulation (MOC) and shifts between these patterns, around the time of the Eocene-Oligocene Transition (EOT) is studied. This is done using the ocean-only, fully implicit thermohaline circulation model (THCM) that directly computes the three-dimensional equilibrium ocean circulation under a change in parameter, such as a perturbation in surface freshwater flux (see section 2.1). Ocean circulation states are obtained for two different paleobathymetries, at 40 Ma and 30 Ma (see section 2.2) with surface forcing patterns taken from equilibrium solutions obtained with 4× (38 Ma) and 2× (30 Ma) pre-industrial CO_2 forcing with the Community Earth System Model (CESM) in Baatsen (2019); Baatsen et al. (2020) (see section 2.3).
Under restoring boundary conditions there seems to be a preference for a strong, fully southern sinking MOC-state. When the upper layer salinity forcing is mirrored in the equator, a strong, fully northern sinking MOC-state is found. Hence the main direction of overturning under restoring boundary conditions seems to be linked to the north-south asymmetry in upper layer salinity, as deep water formation tends to occur in the hemisphere with the most saline waters at high latitude. The strong, fully southern sinking MOC-pattern seems to be relatively dominant, as under mixed boundary conditions no direct connections to other MOC-patterns were found. This could, however, be a numerical effect or a result of asymmetry in the forcing fields and/or bathymetry. Why this isolation of the strong southern sinking MOC-pattern occurs requires further research, for example by repeating the simulations with smoother or more symmetric forcing fields and/or bathymetry.
Bifurcation diagrams of the change in MOC-pattern for a linear deformation between two freshwater flux fields, diagnosed from the strong northern sinking and strong southern sinking MOC-states, which can be interpreted as a complex freshwater flux perturbation, are computed. These bifurcation diagrams are mainly found to consist of one long branch connecting a range of different MOC-patterns, including northern sinking, bipolar sinking and southern sinking patterns. Hence several qualitatively different MOC-patterns are found to occur in the same paleobathymetry and these different patterns can be reached by changing the freshwater flux. Moreover, as multiple MOC-states are found to occur under the same mixed boundary conditions in a large part of the bifurcation diagrams, a switch to another MOC-state induced by only a random perturbation in freshwater flux (in reality this could be due to e.g. random atmospheric fluctuations) could be possible. To see which switches are likely to occur, which of the found MOC-patterns are stable and when they become unstable requires stability analysis, which is a subject for future research.
When considering the qualitatively different MOC-states that occur under the same mixed boundary conditions as the strong northern and southern sinking solutions obtained with restoring boundary conditions, the following is notable. In the MOC-states occurring under the same boundary conditions as the restoring northern sinking solution the overturning direction in the Pacific is northward, while for the MOC-states occurring under the same boundary conditions as the restoring southern sinking solution the overturning direction is southward. For all other basins, especially in the Atlantic, overturning occurs in both directions, independent of the mixed boundary conditions. Thus the overturning direction in the Pacific seems to be determined by the freshwater flux pattern, while this is not the case for the other basins. This dependence of the overturning direction in the Pacific on boundary conditions is probably a result of the Pacific being much larger than the other basins. Furthermore, with the same boundary conditions as the restoring southern sinking solution, and thus southward overturning in the Pacific, only southern sinking solutions are found. With the same boundary conditions as the restoring northern sinking solution, and thus with northward overturning in the Pacific, though, more different MOC-states, including northern sinking, bipolar sinking and southern sinking, seem to be possible. There seems to be no major difference between the MOC-

patterns that are possible for 40 Ma and 30 Ma cases, though more patterns are found for 30 Ma case, which might suggest that a switch in MOC-pattern is more likely with this bathymetry and forcing.
The mixed boundary conditions derived from the restoring southern sinking solution are least modified from the original CESM fields from Baatsen (2019) and are thus most representative of a Late Eocene climate. With these boundary conditions two different types of MOC-states are found: a strong fully southern sinking solution and a solution with slightly weaker southern sinking and weak northern sinking in the Atlantic. The possibility of a shift from the first solution to the second solution seems to agree with the proposed onset of the Atlantic Meridional Overturning Circulation (AMOC) around the time of the EOT (Hutchinson et al., 2020). The global average and deep ocean temperatures show an increase with this shift, which is opposite to the observed cooling around the EOT, though the temperature changes in the model might not give a good representation as they are strongly dependant on the prescribed upper layer temperature field. To understand the effects of such a shift in MOC-pattern on climate requires more research, for example with the model extended to include an (simple) atmosphere and possibly (sea) ice. The global meridional heat transport is observed to be less strongly southward when this shift in MOC-pattern occurs, with more northward heat transport in the northern hemisphere. This suggests that this shift would result in cooler southern high latitudes and warmer northern high latitudes compared to before the shift.

The two cases, 40 Ma bathymetry with 38 Ma 4PIC forcing and 30 Ma bathymetry with 30 Ma 2PIC forcing can be interpreted to represent a range of possible bathymetries and climates around the time of the EOT. In both cases multiple equilibrium MOC-states are found, including northern sinking, bipolar sinking and southern sinking states, that are (almost) all connected under a change in freshwater flux. Furthermore, for a range in freshwater flux forcing patterns, multiple equilibrium MOC-states are found to occur under the same mixed boundary conditions, though which equilibrium MOC-states occur depends on the freshwater flux forcing. Hence a shift from one MOC-pattern to another induced by e.g. small atmospheric fluctuations might be possible around the EOT, specifically a shift from a fully southern sinking MOC-state to a southern sinking MOC-state with weak northern sinking in the Atlantic, which could correspond to the proposed onset of the AMOC at the time of the EOT. As multiple equilibrium MOC-states are found to occur for different bathymetries, CO_2 forcings and freshwater flux forcings, the possibility of a shift between different MOC-states around the time of the EOT seems relatively independent of the exact timing of e.g. gateway openings and the exact climate, e.g. of CO_2 levels.
For future research it would be interesting to repeat the simulations with the forcing fields and/or bathymetry made more smoothly, with the setup slightly more symmetric and/or using a different, more intuitive parameter for the bifurcation diagram. This to see whether this results in a smoother bifurcation diagram and if this removes the isolation of the strong fully southern sinking solution. Other improvements of the simulation could be made by using a more realistic value for the horizontal mixing coefficient of momentum, by including a way to represent convective overturning, by using a more realistic nonlinear equation of state or by increasing the model resolution. Furthermore, the model could be extended to a coupled model by including a (simple) atmosphere and/or by including (sea) ice to study the effect of a MOC-pattern shift on climate, specifically on the Antarctic ice sheet development. Another subject of further study is to investigate the stability of the found solutions, which might yield more information on the preference for one or more MOC-states, which shifts are likely to occur and the mechanisms behind a possible shift.

Acknowledgements

Many thanks to Anna von der Heydt, my supervisor, for her support and feedback. Also, I would like to thank Erik Mulder for his input and help with the model and and Michiel Baatsen for providing me with the surface fields from his CESM simulations.

Bibliography

Baatsen, M., van Hinsbergen, D.J.J., von der Heydt, A.S., Dijkstra, H.A., Sluijs, A., Abels, H.A., and Bijl, P.K. Reconstructing geographical boundary conditions for palaeoclimate modelling during the cenozoic. *Climate of the Past*, 12:1635–1644, 2016. ISSN 1635–1644. doi: {10.5194/cp-12-1635-2016}.

Baatsen, M., von der Heydt, A. S., Huber, M., Kliphuis, M. A., Bijl, P. K., Sluijs, A., and Dijkstra, H. A. The middle to late eocene greenhouse climate modelled using the cesm 1.0.5. *Climate of the Past*, 16(6):2573–2597, 2020. doi: 10.5194/cp-16-2573-2020. URL https://cp.copernicus.org/articles/16/2573/2020/.

Baatsen, M. L. J. *The Middle-to-late Eocene Climate : Simulated using the CESM 1.0.5*. PhD thesis, Utrecht University, 2019.

Baatsen, M.L.J., von der Heydt, A.S., Kliphuis, M., Viebahn, J., and Dijkstra, H.A. Multiple states in the late eocene ocean circulation. *Global and Planetary Change*, 163:18–28, 2018. doi: {10.1016/j.gloplacha.2018.02.009}.

Bohaty, S.M., Zachos, J.C., and Delaney, M.L. Foraminiferal Mg/Ca evidence for Southern Ocean cooling across the Eocene-Oligocene transition. *Earth and Planetary Science Letters*, 317:251–261, FEB 1 2012. ISSN 0012-821X. doi: {10.1016/j.epsl.2011.11.037}.

Borrelli, C., Cramer, B.S., and Katz, M.E. Bipolar atlantic deepwater circulation in the middle-late eocene: Effects of southern ocean gateway openings. *Paleoceanography*, 29(4):308–327, 2014. doi: 10.1002/2012PA002444.

Cheng, W., Chiang, J.C.H., and Zhang, D. Atlantic meridional overturning circulation (amoc) in cmip5 models: Rcp and historical simulations. *Journal of Climate*, 26(18):7187–7197, 2013. doi: 10.1175/JCLI-D-12-00496.1.

Coxall, H.K., Wilson, P.A., Pälike, H., Lear, C.H., and Backman, J. Rapid stepwise onset of Antarctic glaciation and deeper calcite compensation in the Pacific Ocean. *Nature*, 433(7021):53–57, JAN 6 2005. ISSN 0028-0836. doi: {10.1038/nature03135}.

de Niet, A., Wubs, F., Terwisscha van Scheltinga, A., and Dijkstra, H.A. A tailored solver for bifurcation analysis of ocean-climate models. *Journal of Computational Physics*, 227(1):654 – 679, 2007. ISSN 0021-9991. doi: 10.1016/j.jcp.2007.08.006.

DeConto, R.M. and Pollard, D. Rapid Cenozoic glaciation of Antarctica induced by declining atmospheric CO2. *Nature*, 421(6920):245–249, JAN 16 2003. ISSN 0028-0836. doi: {10.1038/nature01290}.

den Toom, M., Dijkstra, H.A., and Wubs, F.W. Spurious multiple equilibria introduced by convective adjustment. *Ocean Modelling*, 38(1-2):126–137, 2011. ISSN 1463-5003. doi: {10.1016/j.ocemod.2011.02.009}.

Dijkstra, H.A. *Dynamical oceanography*. Springer Verlag, 2008. doi: 10.1007/978-3-540-76376-5.

Dijkstra, H.A. *Nonlinear Climate Dynamics*. Cambridge University Press, 2013. doi: 10.1017/CBO9781139034135.

Dijkstra, H.A. Numerical bifurcation methods applied to climate models: analysis beyond simulation. *Nonlinear Processes in Geophysics*, 26(4):359–369, 2019. doi: 10.5194/npg-26-359-2019. URL https://npg.copernicus.org/articles/26/359/2019/.

Dijkstra, H.A. and Weijer, W. Stability of the global ocean circulation: Basic bifurcation diagrams. *Journal of Physical Oceanography*, 35(6):933–948, JUN 2005. ISSN 0022-3670. doi: {10.1175/JPO2726.1}.

Ferreira, D., Cessi, P., Coxall, H.K., de Boer, A., Dijkstra, H.A., Drijfhout, S.S., Eldevik, T., Harnik, N., McManus, J.F., Marshall, D.P., Nilsson, J., Roquet, F., Schneider, T., and Wills, R.C. Atlantic-pacific asymmetry in deep water formation. *Annual Review of Earth and Planetary Sciences*, 46(1):327–352, 2018. doi: 10.1146/annurev-earth-082517-010045. URL https://doi.org/10.1146/annurev-earth-082517-010045.

Fontorbe, G., Frings, P.J., De la Rocha, C.L., Hendry, K.R., Carstensen, J., and Conley, D.J. Enrichment of dissolved silica in the deep equatorial Pacific during the Eocene-Oligocene. *Paleoceanography*, 32(8):848–863, AUG 2017. ISSN 0883-8305. doi: {10.1002/2017PA003090}.

Gill, A.E. *Atmosphere-Ocean Dynamics, Appendix 3*, pages 599–603. Number 30 in International Geophysics Series. Academic Press, 1982. ISBN 9780122835223.

Huber, M. and Nof, D. The ocean circulation in the southern hemisphere and its climatic impacts in the Eocene. *PaleoGeography, Paleoclimatology, Paleoecology*, 231(1-2):9–28, FEB 9 2006. ISSN 0031-0182. doi: {10.1016/j.palaeo.2005.07.037}. 32nd International Geological Congress, Florence, ITALY, AUG 20-28, 2004.

Huisman, S.E., Dijkstra, H.A., von der Heydt, A., and de Ruijter, W. P. M. Robustness of multiple equilibria in the global ocean circulation. *Geophysical Reseach Letters*, 36, JAN 15 2009. ISSN 0094-8276. doi: {10.1029/2008GL036322}.

Huisman, S.E., Dijkstra, H.A., von der Heydt, A.S., and de Ruijter, W.P.M. Does Net E - P Set a Preference for North Atlantic Sinking? *Journal of Physical Oceanography*, 42(11):1781–1792, NOV 2012. ISSN 0022-3670. doi: {10.1175/JPO-D-11-0200.1}.

Hutchinson, D. K., Coxall, H. K., Lunt, D. J., Steinthorsdottir, M., de Boer, A. M., Baatsen, M., von der Heydt, A., Huber, M., Kennedy-Asser, A. T., Kunzmann, L., Ladant, J.-B., Lear, C. H., Moraweck, K., Pearson, P. N., Piga, E., Pound, M. J., Salzmann, U., Scher, H. D., Sijp, W. P., Śliwińska, K. K., Wilson, P. A., and Zhang, Z. The eocene-oligocene transition: a review of marine and terrestrial proxy data, models and model-data comparisons. *Climate of the Past Discussions*, 2020:1–71, 2020. doi: 10.5194/cp-2020-68. URL https://cp.copernicus.org/preprints/cp-2020-68/.

Hutchinson, D.K., de Boer, A.M., Coxall, H.K., Caballero, R., Nilsson, J., and Baatsen, M. Climate sensitivity and meridional overturning circulation in the late eocene using gfdl cm2.1. *Climate of the Past*, 14(6):789–810, 2018. doi: 10.5194/cp-14-789-2018. URL https://www.clim-past.net/14/789/2018/.

Hutchinson, D.K., Coxall, H.K., O'Regan, M., Nilsson, J., Caballero, R., and de Boer, A.M. Arctic closure as a trigger for atlantic overturning at the eocene-oligocene transition. *Nature Communications*, 10(1), 2019. doi: 10.1038/s41467-019-11828-z.

Katsman, C.A., Drijfhout, S.S., Dijkstra, H.A., and Spall, M.A. Sinking of dense north atlantic waters in a global ocean model: Location and controls. *Journal of Geophysical Research: Oceans*, 123(5): 3563–3576, 2018. doi: 10.1029/2017JC013329. URL https://agupubs.onlinelibrary.wiley.com/doi/abs/10.1029/2017JC013329.

Katz, M.E., Miller, K.G., Wright, J.D., Wade, B.S., Browning, J.V., Cramer, B.S., and Rosenthal, Y. Stepwise transition from the Eocene greenhouse to the Oligocene icehouse. *Nature Geoscience*, 1 (5):329–334, MAY 2008. ISSN 1752-0894. doi: {10.1038/ngeo179}.

Keller, H. B. Numerical solution of bifurcation and nonlinear eigenvalue problems. *In: Applications of Bifurcation Theory (Proc. Advanced Sem., Univ. Wisconsin, Madison, Wis., 1976)*. *Academic Press, New York, pp. 359-384. Publ. Math. Res. Center, No 38.*, 1977.

Lear, C.H., Bailey, T.R., Pearson, P.N., Coxall, H.K., and Rosenthal, Y. Cooling and ice growth across the Eocene-Oligocene transition. *Geology*, 36(3):251–254, MAR 2008. ISSN 0091-7613. doi: {10.1130/G24584A.1}.

Livermore, R., Nankivell, A., Eagles, G., and Morris, P. Paleogene opening of Drake Passage. *Earth and Planetary Science Letters*, 236(1-2):459–470, JUL 30 2005. ISSN 0012-821X. doi: {10.1016/j.epsl.2005.03.027}.

McKinley, C.C., Thomas, D.J., LeVay, L.J., and Rolewicz, Z. Nd isotopic structure of the pacific ocean 40–10 ma, and evidence for the reorganization of deep north pacific ocean circulation between 36 and 25 ma. *Earth and Planetary Science Letters*, 521:139–149, 2019. doi: 10.1016/j.epsl.2019.06.009.

Mulder, T.E., Baatsen, M.L.J., Wubs, F.W., and Dijkstra, H.A. Efficient computation of past global ocean circulation patterns using continuation in paleobathymetry. *Ocean Modelling*, 115:77–85, JUL 2017. ISSN 1463-5003. doi: {10.1016/j.ocemod.2017.05.010}.

Pälike et al., H. A Cenozoic record of the equatorial Pacific carbonate compensation depth. *Nature*, 488(7413):609+, AUG 30 2012. ISSN 0028-0836. doi: {10.1038/nature11360}.

Pearson, P.N., Foster, G.L., and Wade, B.S. Atmospheric carbon dioxide through the Eocene-Oligocene climate transition. *Nature*, 461(7267):1110–U204, OCT 22 2009. ISSN 0028-0836. doi: {10.1038/nature08447}.

Pfuhl, H.A. and McCave, I.N. Evidence for late Oligocene establishment of the Antarctic Circumpolar Current. *Earth and Planetary Science Letters*, 235(3-4):715–728, JUL 15 2005. ISSN 0012-821X. doi: {10.1016/j.epsl.2005.04.025}.

Prothero, Donald R. The late eocene-oligocene extinctions. *Annual Review of Earth and Planetary Sciences*, 22(1):145–165, 1994. doi: 10.1146/annurev.ea.22.050194.001045. URL https://doi.org/10.1146/annurev.ea.22.050194.001045.

Sabine, C.L., Feely, R.A., Gruber, N., Key, R.M., Lee, K., Bullister, J.L., Wanninkhof, R., Wong, C.S., Wallace, D.W.R., Tilbrook, B., Millero, F.J., Peng, T.-H., Kozyr, A., Ono, T., and Rios, A.F. The oceanic sink for anthropogenic co2. *Science*, 305(5682):367–371, 2004. doi: 10.1126/science.1097403.

Scher, H.D. and Martin, E.E. Timing and climatic consequences of the opening of Drake Passage. *Science*, 312(5772):428–430, APR 21 2006. ISSN 0036-8075. doi: {10.1126/science.1120044}.

Sluijs, S., A .and Schouten, Pagani, M., Woltering, M., Brinkhuis, H., Damste, J.S.S., Dickens, G.R., Huber, M., Reichart, G.J., Stein, R., Matthiessen, J., Lourens, L.J., Pedentchouk, N., Backman, J., Moran, K., and Scientists, Expedition 302. Subtropical arctic ocean temperatures during the Palaeocene/Eocene thermal maximum. *Nature*, 441(7093):610–613, JUN 1 2006. ISSN 0028-0836. doi: {10.1038/nature04668}.

Stanley, S.M. *Earth System History*, pages 444–445. W.H. Freeman, 2008.

Thies, J., Wubs, F., and Dijkstra, H.A. Bifurcation analysis of 3d ocean flows using a parallel fully-implicit ocean model. *Ocean Modelling*, 30(4):287 – 297, 2009. ISSN 1463-5003. doi: https://doi.org/10.1016/j.ocemod.2009.07.005. URL http://www.sciencedirect.com/science/article/pii/S1463500309001553.

Thomas, D.J., L., Mitchell, Moore, T.C., and Rea, D.K. Paleogene deepwater mass composition of the tropical pacific and implications for thermohaline circulation in a greenhouse world. *Geochemistry, Geophysics, Geosystems*, 9(2):n/a–n/a, 2008. ISSN 1525-2027. doi: 10.1029/2007GC001748. Q02002.

Tigchelaar, M., von der Heydt, A.S., and Dijkstra, H.A. A new mechanism for the two-step delta O-18 signal at the Eocene-Oligocene boundary. *Climate of the Past*, 7(1):235–247, 2011. ISSN 1814-9324. doi: {10.5194/cp-7-235-2011}.

Via, R.K. and Thomas, D.J. Evolution of Atlantic thermohaline circulation: Early Oligocene onset of deep-water production in the North Atlantic. *Geology*, 34(6):441–444, JUN 2006. ISSN 0091-7613. doi: {10.1130/G22545.1}.

von der Heydt, A. and Dijkstra, H.A. The effect of gateways on ocean circulation patterns in the Cenozoic. *Global and Planetary Change*, 62(1-2):132–146, MAY 2008. ISSN 0921-8181. doi: {10.1016/j.gloplacha.2007.11.006}.

Westerhold, T., Marwan, N., Drury, A.J., Liebrand, D., Agnini, C., Anagnostou, E., Barnet, J.S.K., Bohaty, S.M., De Vleeschouwer, D., Florindo, F., Frederichs, T., Hodell, D.A., Holbourn, A.E., Kroon, D., Lauretano, V., Littler, K., Lourens, L.J., Lyle, M., Pälike, H., Röhl, U., Tian, J., Wilkens, R.H., Wilson, P.A., and Zachos, J.C. An astronomically dated record of earth's climate and its predictability over the last 66 million years. *Science*, 369(6509):1383–1388, 2020. doi: 10.1126/SCIENCE.ABA6853.

Zachos, J., Pagani, M., Sloan, L., Thomas, E., and Billups, K. Trends, rhythms, and aberrations in global climate 65 Ma to present. *Science*, 292(5517):686–693, APR 27 2001. ISSN 0036-8075. doi: {10.1126/science.1059412}.

A Overturning streamfunction per basin

This appendix includes plots of the meridional overturning streamfunction per basin and globally for the steady state solution indicated in the figure caption. Solution labels correspond to the labels in Table 3.1 and Table 3.2 and to the letters in Figure 3.7 and Figure 3.8. The minimum and maximum of the overturning streamfunction are calculated below a depth of 500 m. Contours are drawn at an interval of respectively 5 Sv and are indicated on the colorbar.

A.1 Steady states under restoring boundary conditions

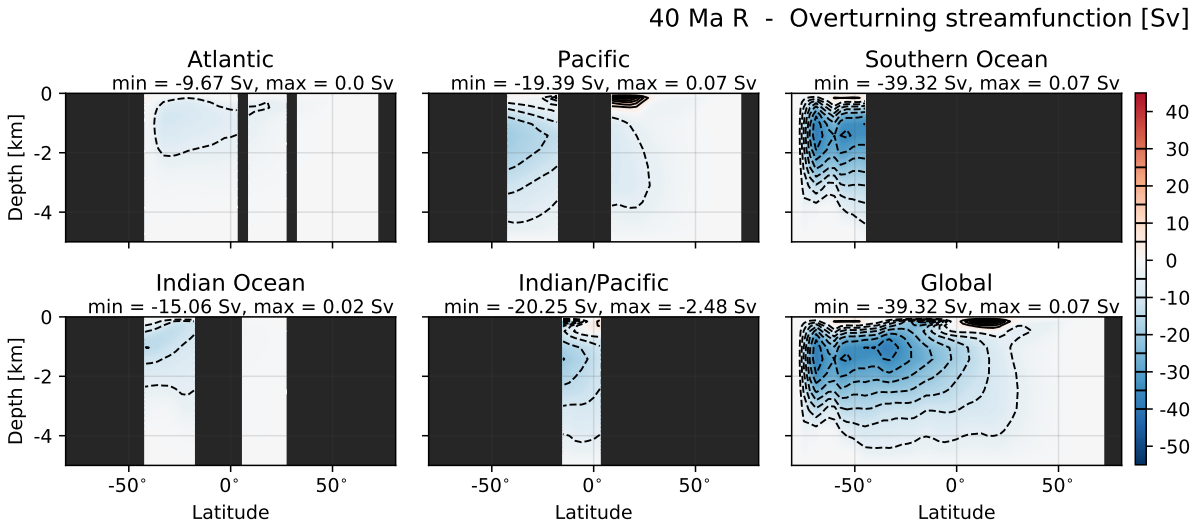

Figure A.1: Restoring solution for 40 Ma bathymetry under 38Ma 4PIC forcing (40 Ma R, see Figure 3.1).

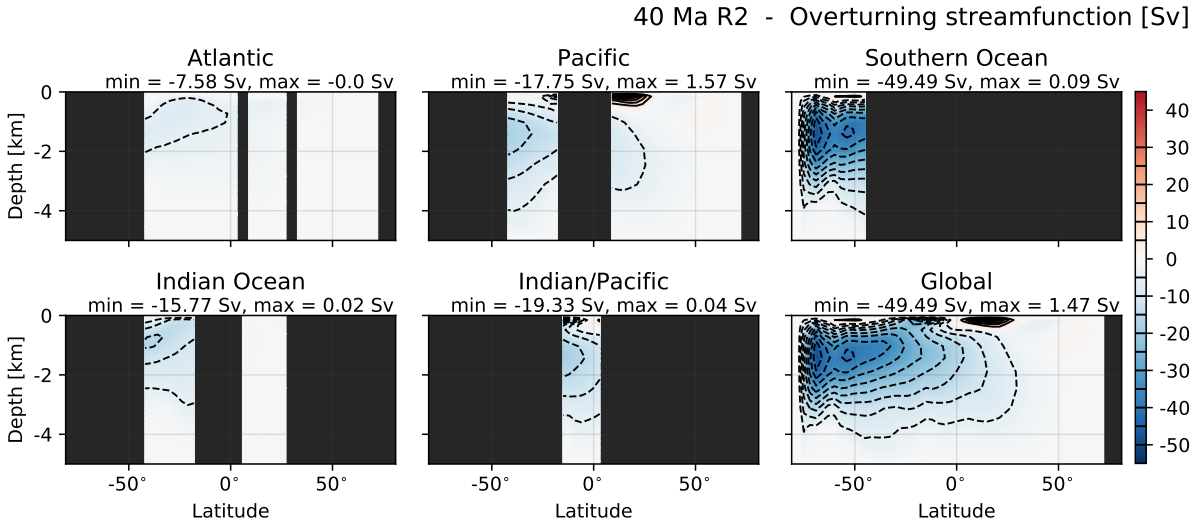

Figure A.2: Restoring solution for 40 Ma bathymetry under 38Ma 2PIC forcing (40 Ma R2, see Figure 3.3).

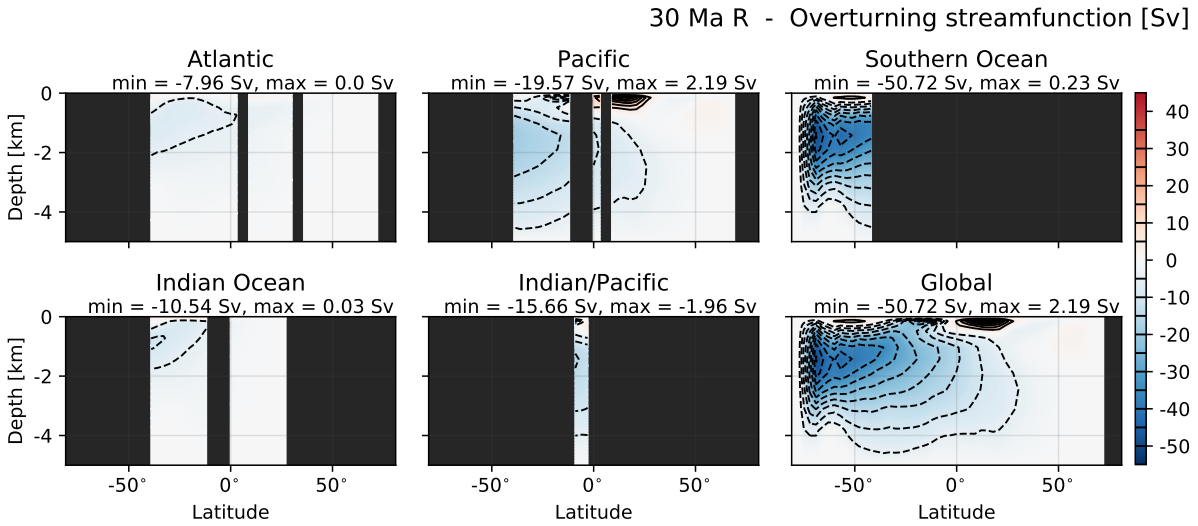

Figure A.3: Restoring solution for 30 Ma bathymetry under 30Ma 2PIC forcing (30 Ma R, see Figure 3.2).

A.2 Steady states under modified salinity forcing

A.2.1 40 Ma

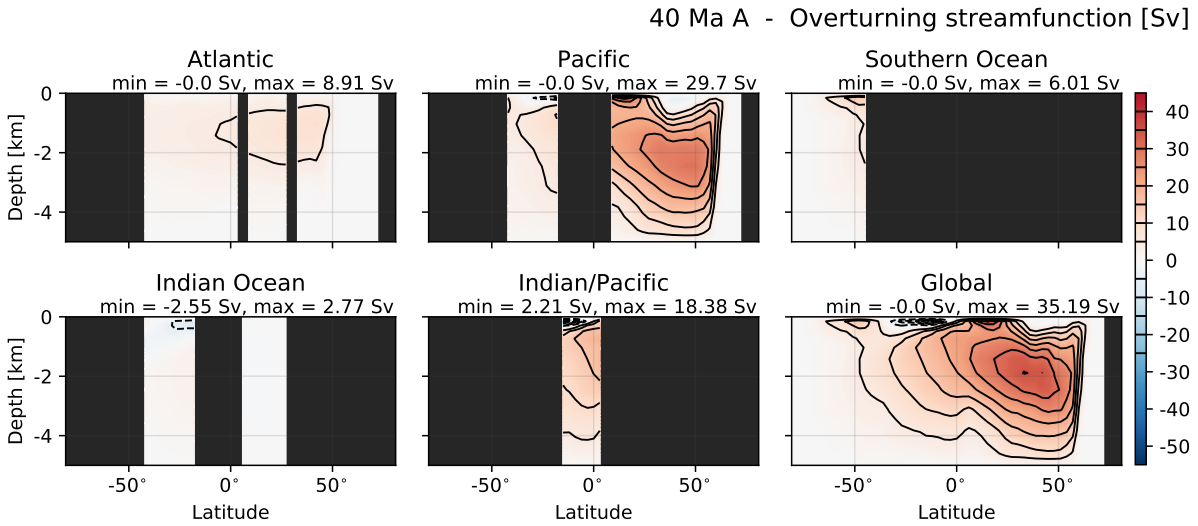

Figure A.4: Solution for 40 Ma bathymetry under modified forcing (40 Ma A, see Figure 3.7A).

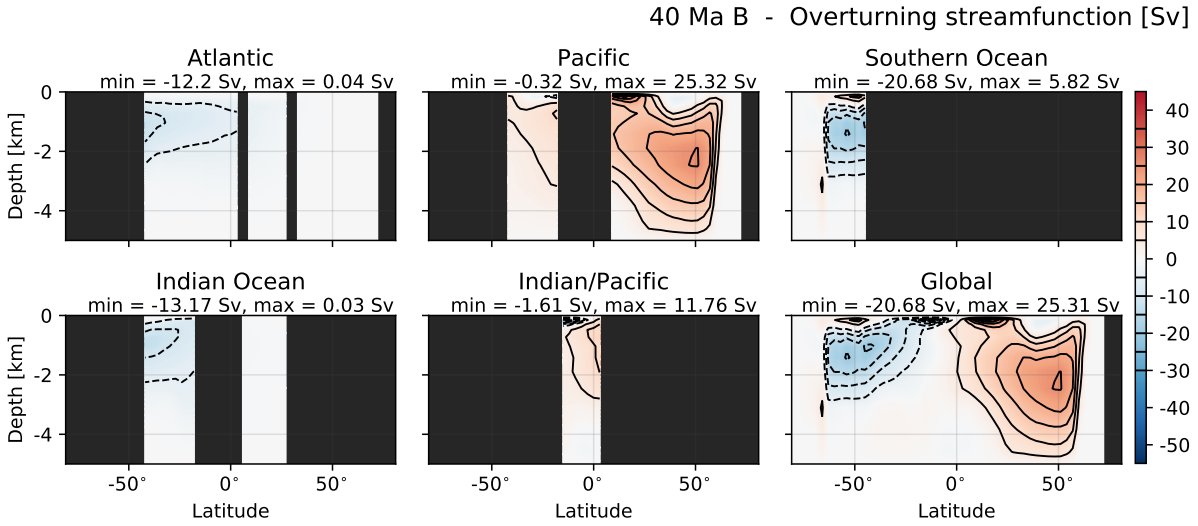

Figure A.5: Solution for 40 Ma bathymetry under modified forcing (40 Ma B, see Figure 3.7B).

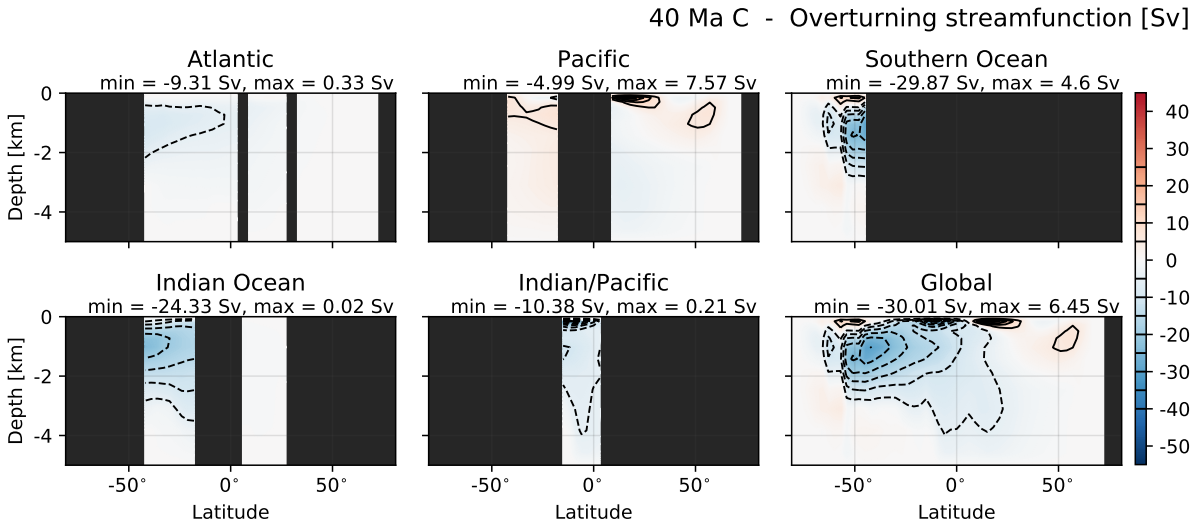

Figure A.6: Solution for 40 Ma bathymetry under modified forcing (40 Ma C, see Figure 3.7C).

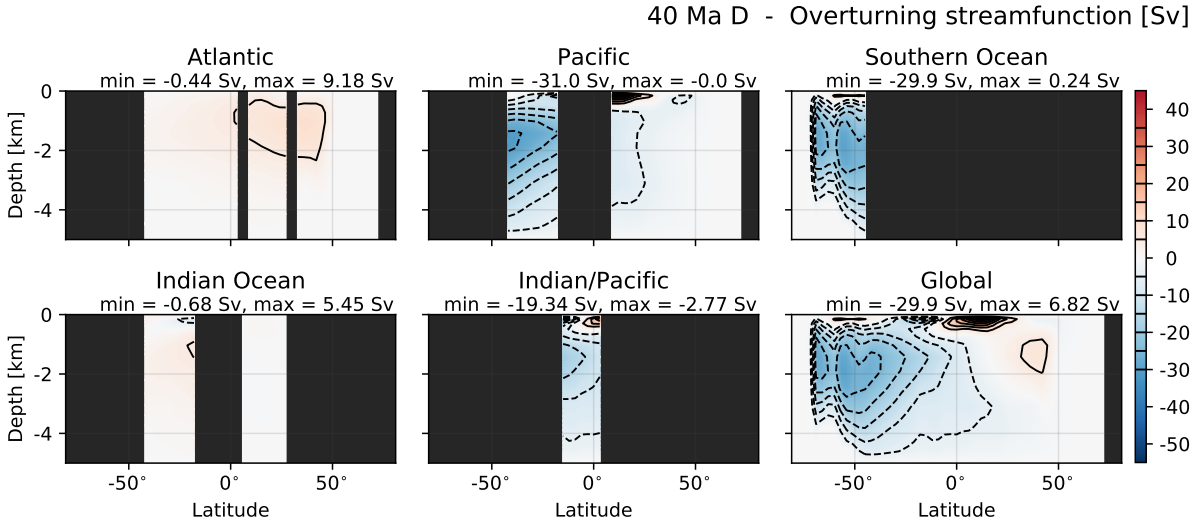

Figure A.7: Solution for 40 Ma bathymetry under modified forcing (40 Ma D, see Figure 3.7D).

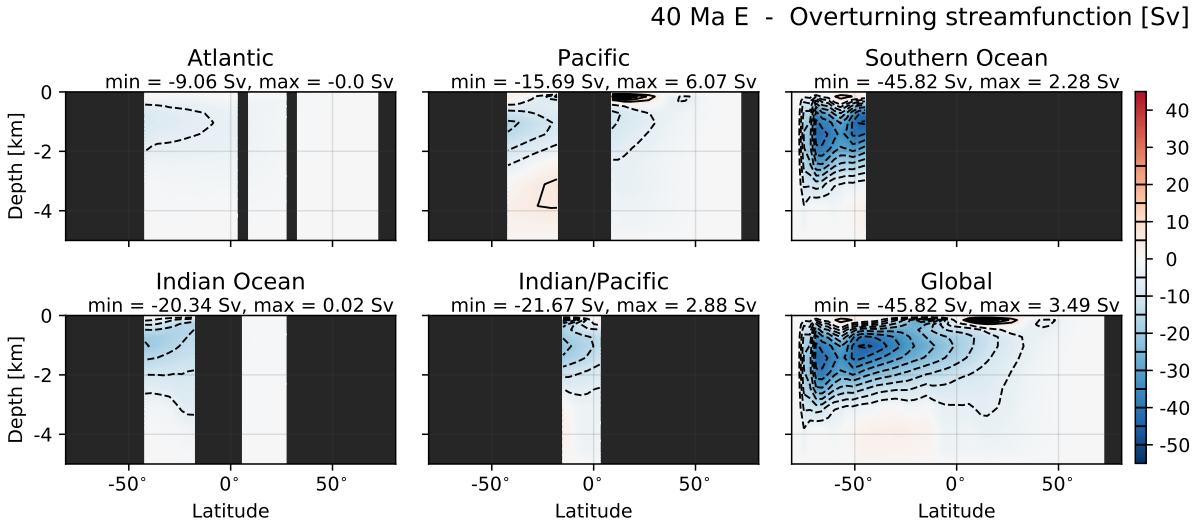

Figure A.8: Solution for 40 Ma bathymetry under modified forcing (40 Ma E, see Figure 3.7E).

A.2.2 30 Ma

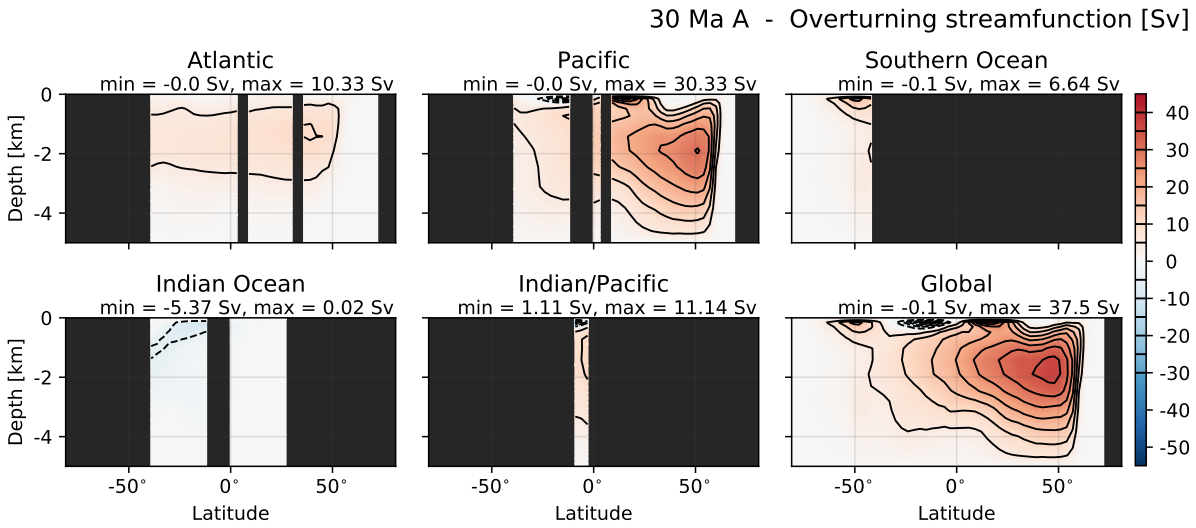

Figure A.9: Solution for 30 Ma bathymetry under modified forcing (30 Ma A, see Figure 3.8A).

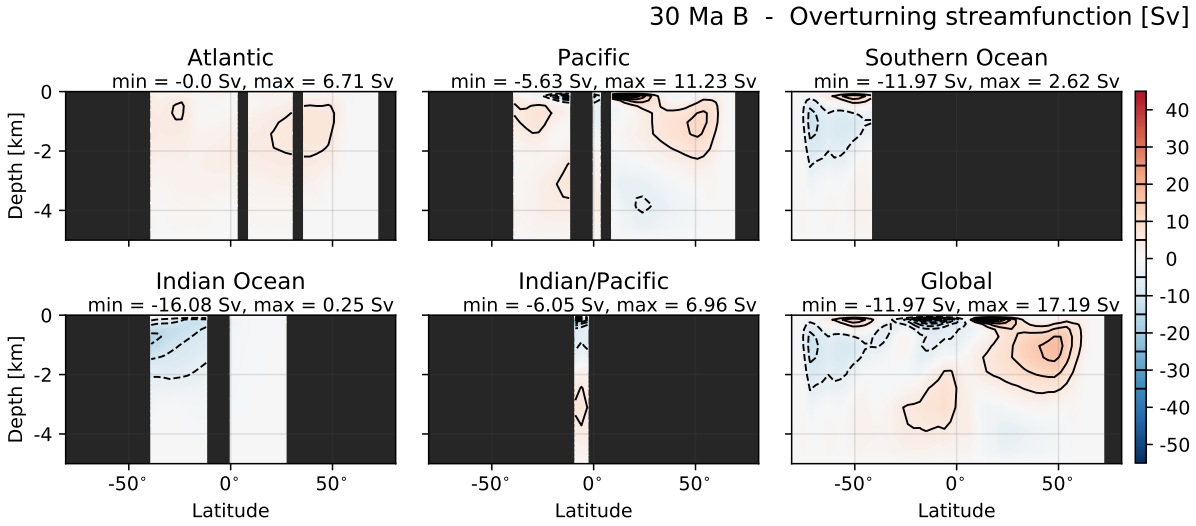

Figure A.10: Solution for 30 Ma bathymetry under modified forcing (30 Ma B, see Figure 3.8B).

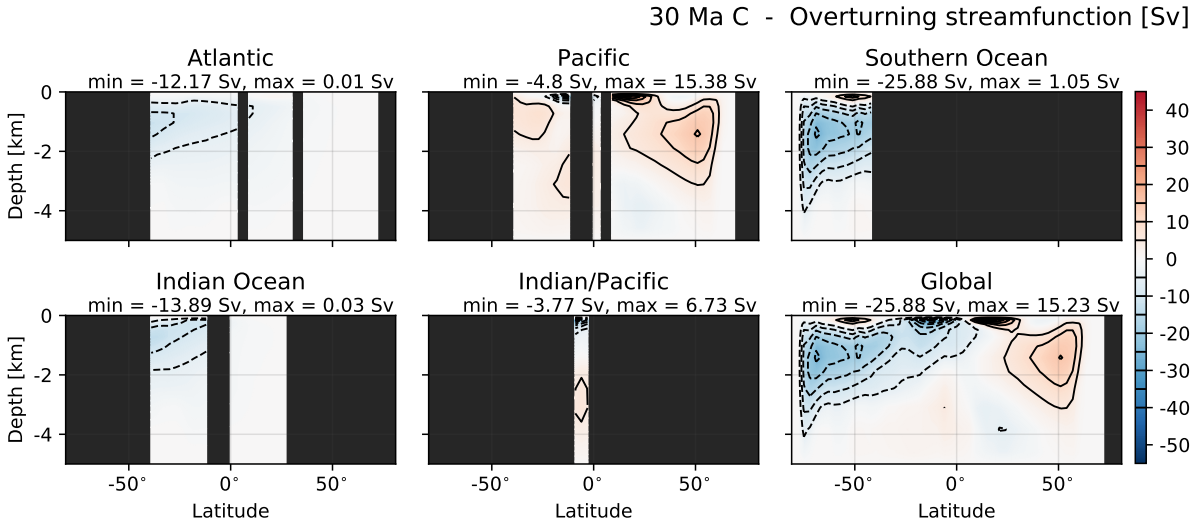

Figure A.11: Solution for 30 Ma bathymetry under modified forcing (30 Ma C, see Figure 3.8C).

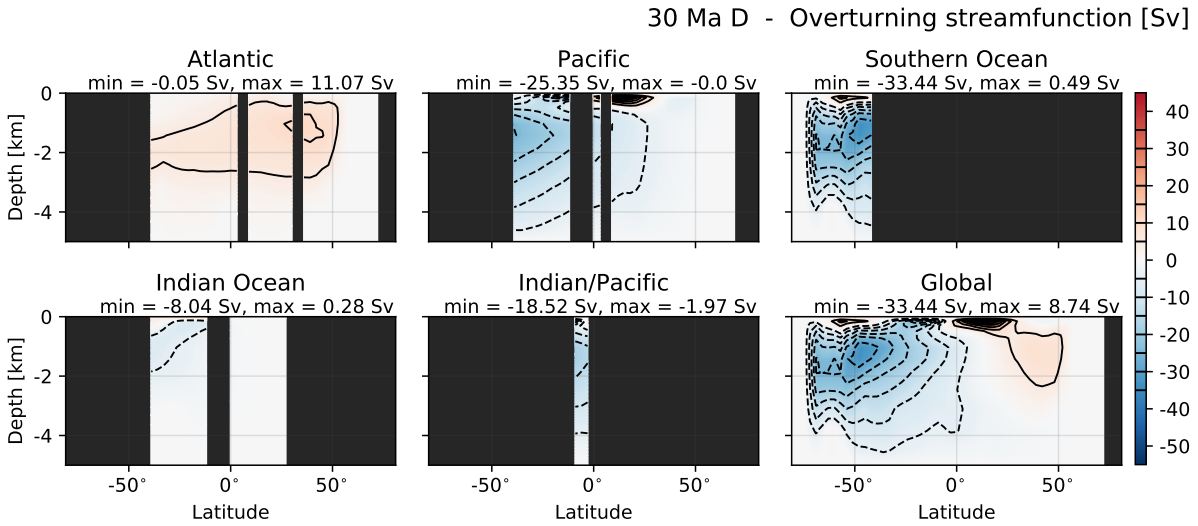

Figure A.12: Solution for 30 Ma bathymetry under modified forcing (30 Ma D, see Figure 3.8D).

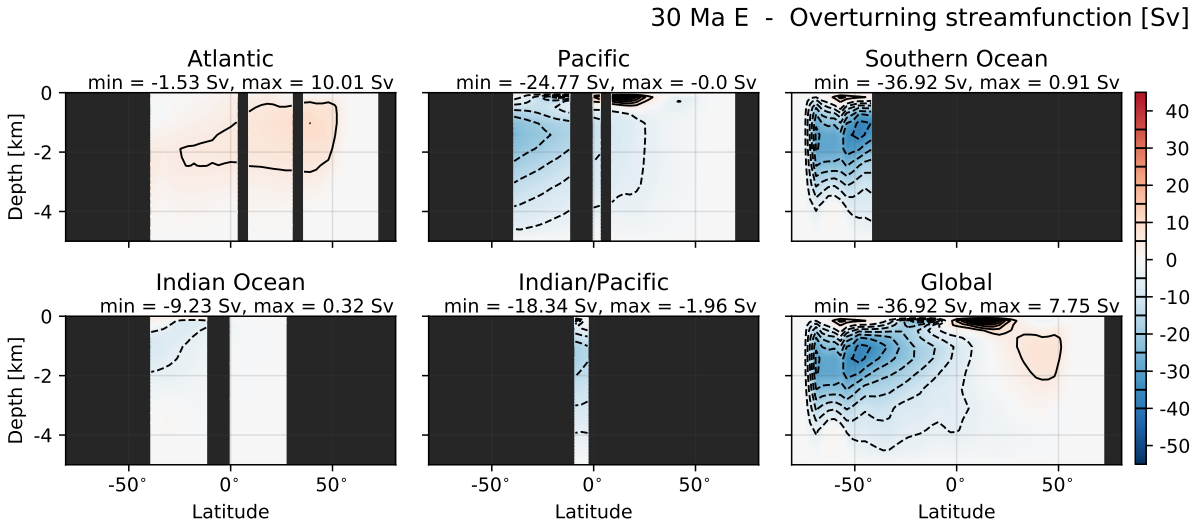

Figure A.13: Solution for 30 Ma bathymetry under modified forcing (30 Ma E, see Figure 3.8E).

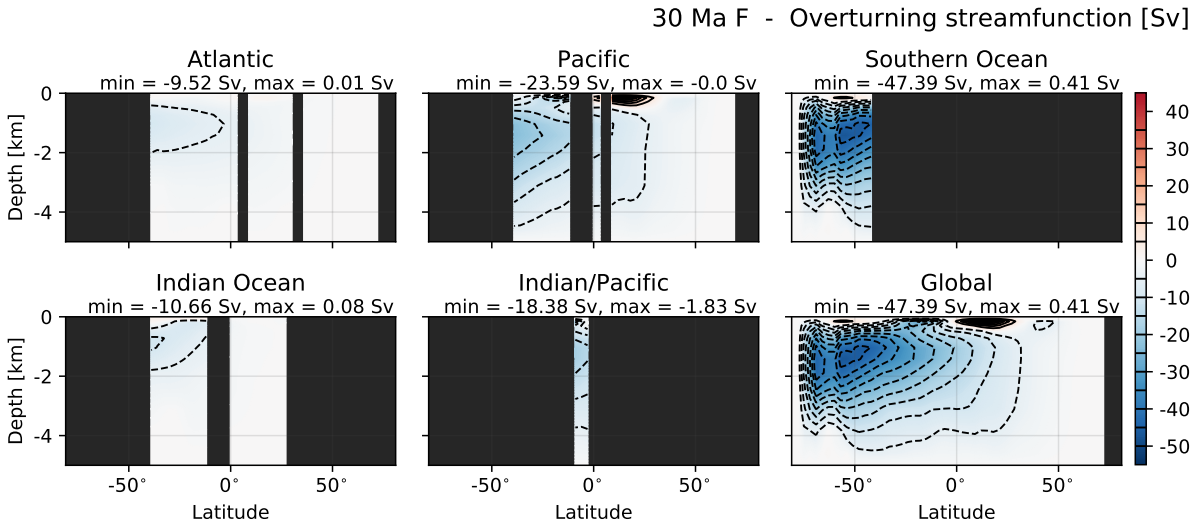

Figure A.14: Solution for 30 Ma bathymetry under modified forcing (30 Ma F, see Figure 3.8F).